Numerical Study of Nocturnal Low-Level Jets over Gently Sloping Terrain

EVGENI FEDOROVICH

School of Meteorology, University of Oklahoma, Norman, Oklahoma

JEREMY A. GIBBS

Cooperative Institute for Mesoscale Meteorological Studies, University of Oklahoma, Norman, Oklahoma, and Department of Mechanical Engineering, University of Utah, Salt Lake City, Utah

ALAN SHAPIRO

School of Meteorology, and Center for Analysis and Prediction of Storms, University of Oklahoma, Norman, Oklahoma

(Manuscript received 18 January 2017, in final form 15 June 2017)

ABSTRACT

Nocturnal low-level jets (LLJs) over gently sloping terrain typical of the U.S. Great Plains are investigated by means of direct numerical simulation. Such LLJs develop in a tilted atmospheric boundary layer as a result of inertia–gravity oscillations initiated by a change of the surface thermal forcing during the evening transition. External parameters are the free-atmospheric geostrophic wind, ambient atmospheric stratification, surface buoyancy forcing, and slope angle. The governing momentum and buoyancy balance equations are written in slope-following coordinates, and solved numerically in the Boussinesq approximation. The surface forcing is prescribed in a form of surface buoyancy or buoyancy flux, both of which are slope-uniform but change in time. LLJs over slopes are contrasted with LLJs over flat terrain.

Slope-induced effects essentially modify the entire structure of nocturnal LLJs. The shape of the LLJ wind profile over a slope is characterized by a sharper and larger-magnitude maximum. The presence of the slope causes the along-slope advection of environmental potential temperature during the night. This advection can reignite static instability in the LLJ flow developing after the evening transition. The resulting turbulence leads to a complete or partial remix of the boundary layer flow and drastically changes the appearance of the LLJ in terms of its shape and vertical position. A pronounced nighttime jet can also develop from the daytime convective boundary layer in the absence of any free-atmospheric geostrophic forcing. The daytime flow preconditioning, an important precursor of the nocturnal LLJ development, plays an especially important role in LLJs over a slope.

1. Introduction

The nocturnal low-level jet (LLJ) is an atmospheric boundary layer wind maximum that typically develops under dry and clear conditions after sunset. The jet reaches a peak magnitude a few hours after midnight, and then decays after sunrise with the onset of convective mixing (Shapiro and Fedorovich 2010). LLJs have been observed in many locations throughout the world (see, e.g., Stensrud 1996; Baas et al. 2009; Van de Wiel et al. 2010) but have been most extensively documented over the Great Plains of the United States (e.g., Blackadar 1957; Hoecker 1963; Bonner 1968; Parish et al. 1988; Mitchell et al. 1995; Zhong et al. 1996; Whiteman et al. 1997; Banta et al. 2002; Song et al. 2005; Banta 2008; Walters et al. 2008; Klein et al. 2016).

The LLJ wind speed profile has a pronounced maximum that typically occurs at levels within 500 m above the ground. The maximum wind often exceeds the free-atmosphere geostrophic value by up to 70%. However, significantly stronger LLJs have also been reported (see Hoecker 1963; Bonner 1968; Brook 1985). Great Plains LLJs are often associated with strong southerly geostrophic winds resulting from dominant westward-directed pressure gradients. Such jets can support the development or maintenance of nocturnal convection (Cotton et al.

Corresponding author: Evgeni Fedorovich, fedorovich@ou.edu

DOI: 10.1175/JAS-D-17-0013.1

1989; Augustine and Caracena 1994; Stensrud 1996; Zhong et al. 1996; Higgins et al. 1997; Arritt et al. 1997; Tuttle and Davis 2006; Wang and Chen 2009).

Suggested theories of the LLJ point to the jet being a result of the force imbalance in the atmospheric boundary layer induced by the sudden release of the frictional constraint near sunset (Blackadar 1957). In the case when the synoptic-scale pressure gradient is the dominant forcing, the atmospheric flow response to the force imbalance happens in a form of inertial oscillation. The frictional stress, which was not explicitly considered in the Blackadar analysis, was included in the follow-up study by Buajitti and Blackadar (1957), where the eddy viscosity was varying in time and height. Thorpe and Guymer (1977), Singh et al. (1993), Davies (2000), and Shapiro and Fedorovich (2010) further modified Blackadar's inertial-oscillation theory, mostly by considering a variety of stress parameterizations and eddy-viscosity time dependencies.

Over sloping terrain, however, the along-slope component of the buoyancy force associated with daytime heating and nighttime cooling of the surface can become an important secondary forcing mechanism. Using scale analysis, one may show that the slope angle needs only to be on the order of 0.1° to 0.2°, which is typical of the slope of the Great Plains, in order for the component of buoyancy in the along-slope equation of motion to be of the same order of magnitude as a typical LLJ acceleration required to attain, say, $5\,\mathrm{m\,s^{-1}}$ wind over 6 h. Shapiro and Fedorovich (2009) and Shapiro et al. (2016) pointed to the existence of small slope angles optimal for the generation of strong jets. Accordingly, we view the shallowness of the terrain slope in our study as an important aspect of nocturnal LLJs over the Great Plains.

Although the Blackadar (1957) description of an LLJ with a wind vector that veers in time has been generally confirmed qualitatively, more detailed analyses of observed jets suggest that the theory may be incomplete, or in some cases the considered effects may be of secondary importance [see, e.g., the discussion in Shapiro and Fedorovich (2009)]. For example, Blackadar's theory cannot explain how peak wind speeds in some observed LLJs can reach twice the free-atmospheric geostrophic speed. It also fails to explain the higher frequency of stronger LLJs formed over the gently sloping terrain of the Great Plains. In addition, as discussed in Van de Wiel et al. (2010), a well-mixed late-afternoon atmospheric boundary layer would have a more height-uniform wind distribution than the one indicated in Blackadar's schematic diagram.

Seeking an explanation for the geographical preference of the Great Plains LLJ (around the longitude of 100°W), Holton (1967) demonstrated that the response of the flow over a sloping surface to volumetric heating prescribed as a diurnal harmonic function (with eddy viscosity taken constant in time and height) was a boundary layer wind oscillation. However, the phase of the oscillation was not captured correctly, and the resulting jet profile was not very realistic. Bonner and Paegle (1970) associated the periodicity of the geostrophic wind and eddy viscosity with the diurnal temperature cycle over sloping terrain. However, their analysis did not explicitly take into account the terrain slope or make provision for a thermal energy balance, as the Holton (1967) model did. Their results were in reasonable agreement with observations but were very sensitive to the controlling flow parameters.

Another suggested explanation for the geographical preference of the Great Plains LLJ dates back to Wexler (1961), who described the Great Plains LLJ as a northward inertial boundary layer flow caused by the blocking of the easterly trade winds by the Rocky Mountains. Ting and Wang (2006), Pan et al. (2004), and Jiang et al. (2007) indeed point to such blocking as the dominant mechanism for maintaining the strong southerly large-scale flow over the Great Plains. However, Parish and Oolman (2010) argue that the persistent southerly summer flow over the Great Plains is due to heating of the sloping terrain rather than due to the mechanical blocking.

In Shapiro and Fedorovich (2009), an inviscid-flow theory was proposed to describe the combined effect of terrain slope, thermal boundary layer structure, environmental stratification, and synoptic-scale pressure gradient on the evolution of LLJs. The concept of a tilted (slope-following) residual layer was introduced by analogy to the notion of residual layer over a flat terrain (Stull 1988) to identify conditions favorable for the Great Plains LLJ development. The proposed theory indicated that high supergeostrophic wind speeds often observed in Great Plains LLJs could be explained by the effects of sloping terrain and initial parcel buoyancy. The theoretical prediction also agreed with climatological studies of the Great Plains LLJ on the existence of an optimal slope angle associated with peak jet strength.

Recently, Shapiro et al. (2016) combined the Blackadar (1957), Holton (1967), and Shapiro and Fedorovich (2009, 2010) LLJ theories to incorporate the gentle slope effect through the explicit coupling of the equations of motion and thermal energy balance in the Boussinesq approximation. The setup considered was typical of LLJs over the Great Plains: southerly geostrophic wind over terrain that gently slopes down toward the east. Diurnally periodic solutions, obtained analytically, were controlled by 11 parameters: slope angle, Coriolis parameter, free-atmosphere Brunt–Väisälä frequency, free-atmosphere geostrophic wind, radiative damping parameter, day and night diffusivities (assumed equal for momentum and buoyancy), maximum and minimum surface buoyancies, and times of maximum

surface buoyancy and sunset. The unified theory predicted that jets strengthen with increasing geostrophic wind, maximum surface buoyancy, and day-to-night ratio of the eddy diffusivities, and weaken with increasing Brunt–Väisälä frequency and magnitude of minimum slope buoyancy. Peak winds were found to be maximized for the slope angles characteristic of the Great Plains.

The present study of LLJs is based on the direct numerical simulation (DNS) approach. In recent years, DNS has become a viable tool to study idealized atmospheric boundary layer flows under a variety of stratification and forcing conditions, albeit at relatively low Reynolds numbers (see, e.g., Coleman et al. 1990; Spalart et al. 2008; Shapiro and Fedorovich 2008; Fedorovich and Shapiro 2009b; Marlatt et al. 2012; Mellado 2012; Jonker et al. 2013; Ansorge and Mellado 2014; Garcia and Mellado 2014; Van Heerwaarden et al. 2014; Shah and Bou-Zeid 2014; Deusebio et al. 2014; Van Heerwaarden and Mellado 2016; Mellado et al. 2016). Our study is the first DNS investigation of LLJs over a shallow slope. Although it is highly idealized with respect to some basic components of the simulation setup, it adds much more realism to the LLJ description compared to our preceding analytical study (Shapiro et al. 2016). Specifically, the DNS approach allows us to investigate the role of turbulence in jet formation and evolution, and to explore a suite of physical interactions and feedbacks in the LLJ flow system.

Like Shapiro et al. (2016), this study focuses on the type of LLJ flow characteristic of the Great Plains, where LLJs are predominantly southerly and occur over terrain that gently slopes down toward the east. Because of the presence of the slope, the LLJ develops as a result of an inertia–gravity oscillation in a tilted atmospheric boundary layer. The oscillation is initiated by an abrupt change of the surface thermal forcing during the evening transition. In the simulations, this forcing is prescribed in the form of a slope-uniform but time-varying surface buoyancy or surface buoyancy flux. The simulated turbulence adjusts to the changing thermal conditions in accord with the full governing equations. Among other investigated controlling parameters of the flow are the free-atmosphere geostrophic wind magnitude, the atmospheric stratification prescribed in terms of the environmental buoyancy frequency, and the slope angle. In particular, southerly LLJs over slopes are contrasted with southerly LLJs over flat terrain.

The layout of the paper is as follows. In section 2, the governing equations are presented and explained. The scaled governing equations are introduced in section 3, where rescaling of the simulated flow to atmospheric dimensions is also discussed. The employed numerical algorithm and simulation setups are described in section 4. Section 5 contains analyses of the simulated flow cases for different LLJ evolution scenarios with a focus on the sensitivity of the flow to surface forcing and slope angle. The special case of jet development in the absence of an external geostrophic forcing is also considered. A summary and conclusions follow in section 6.

2. Governing equations for boundary layer flow on a slope

We consider an atmospheric boundary layer flow along a shallow planar slope representing the gently sloping terrain of the Great Plains (see Fig. 1). The Boussinesq-approximated governing equations for this flow are analogous to the slope-flow equations in Fedorovich and Shapiro (2009b) with Coriolis and geostrophic forcing terms included in the momentum balance equations (Shapiro et al. 2016):

$$\frac{\partial u}{\partial t}+u\frac{\partial u}{\partial x}+v\frac{\partial u}{\partial y}+w\frac{\partial u}{\partial z}=-\frac{\partial \pi}{\partial x}+f(v-V_g)-b\sin\alpha+\nu\left(\frac{\partial^2 u}{\partial x^2}+\frac{\partial^2 u}{\partial y^2}+\frac{\partial^2 u}{\partial z^2}\right), \quad (1)$$

$$\frac{\partial v}{\partial t}+u\frac{\partial v}{\partial x}+v\frac{\partial v}{\partial y}+w\frac{\partial v}{\partial z}=-\frac{\partial \pi}{\partial y}-fu+\nu\left(\frac{\partial^2 v}{\partial x^2}+\frac{\partial^2 v}{\partial y^2}+\frac{\partial^2 v}{\partial z^2}\right), \quad (2)$$

$$\frac{\partial w}{\partial t}+u\frac{\partial w}{\partial x}+v\frac{\partial w}{\partial y}+w\frac{\partial w}{\partial z}=-\frac{\partial \pi}{\partial z}+b\cos\alpha+\nu\left(\frac{\partial^2 w}{\partial x^2}+\frac{\partial^2 w}{\partial y^2}+\frac{\partial^2 w}{\partial z^2}\right). \quad (3)$$

The thermal energy (buoyancy balance) and mass conservation (continuity) equations are, respectively,

$$\frac{\partial b}{\partial t}+u\frac{\partial b}{\partial x}+v\frac{\partial b}{\partial y}+w\frac{\partial b}{\partial z}=N^2(u\sin\alpha-w\cos\alpha)+\nu_h\left(\frac{\partial^2 b}{\partial x^2}+\frac{\partial^2 b}{\partial y^2}+\frac{\partial^2 b}{\partial z^2}\right), \quad (4)$$

$$\frac{\partial u}{\partial x}+\frac{\partial v}{\partial y}+\frac{\partial w}{\partial z}=0. \quad (5)$$

Here, $u = v_1$, $v = v_2$, and $w = v_3$ are the velocity components in a right-hand slope-following Cartesian coordinate system $x = x_1$, $y = x_2$, and $z = x_3$ where the x coordinate axis is directed eastward and the y coordinate axis is directed northward (Figs. 1 and 2); $\pi = (p - p_e)/\rho_r$ is the normalized pressure perturbation (p_e is the environmental pressure, which is a function of the true vertical coordinate z' only, and ρ_r = const is the reference density); $b = g[\Theta - \Theta_e(z')]/\Theta_r$ is the buoyancy, where Θ is the potential temperature,

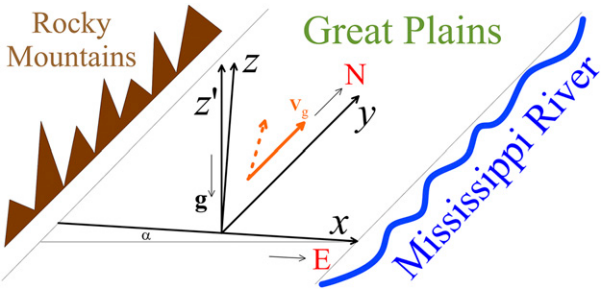

FIG. 1. Schematic of simulation setup for LLJs over the Great Plains. The southern geostrophic wind is indicated by the solid orange arrow and the near-surface wind in the developed daytime convectively mixed layer is schematically presented by the dashed orange arrow.

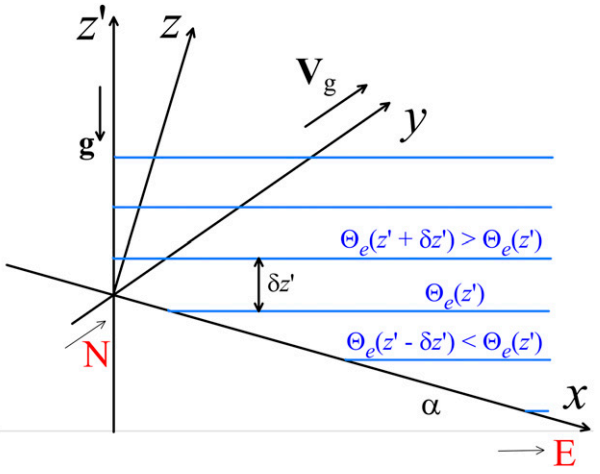

FIG. 2. Slope-following coordinate system and environmental isentropes.

$\Theta_e(z')$ is the environmental potential temperature (Fig. 2), Θ_r = const is the reference potential temperature, and g is the gravity acceleration; f is the Coriolis parameter; $V_g \geq 0$ is the constant free-atmosphere southerly geostrophic wind; $N = [(g/\Theta_r)(d\Theta_e/dz')]^{1/2}$ is the prescribed environmental Brunt–Väisälä (or buoyancy) frequency; α is the slope angle; ν is the kinematic viscosity; and ν_h is the thermal diffusivity. As in Shapiro et al. (2016), we take $\nu_h = \nu$ (Prandtl number $\mathrm{Pr} = \nu/\nu_h = 1$) and consider LLJ dynamics in the Northern Hemisphere ($f > 0$).

The boundary conditions for the prognostic variables (u, v, w, b) and the normalized pressure π in the lateral directions x and y are periodic. The upper boundary conditions (set at sufficiently large z) are $\partial\varphi/\partial z = 0$, where φ is any of (u, v, b), $w = 0$, with $\partial\pi/\partial z$ expressed from the third equation of motion (3). Conditions at the sloping surface ($z = 0$) are no-slip and impermeability ($u = v = w = 0$), with $\partial\pi/\partial z$ prescribed from (3) as in Shapiro et al. (2015), where details on the implementation of condition for pressure are presented in their appendix A. Surface conditions for the buoyancy are specified either as $b|_{z=0} = b_{s1} > 0$ for $t < t_t$ and $b|_{z=0} = b_{s2} > b_{s1}$ for $t \geq t_t$ (surface buoyancy condition), or as $-\nu_h(\partial b/\partial z|_{z=0} = B_{s1} > 0$ for $t < t_t$ and $-\nu_h(\partial b/\partial z|_{z=0} = B_{s2} < 0$ for $t \geq t_t$ (surface buoyancy flux condition), where B denotes the z component of the buoyancy flux, the subscripts s and t stand for surface and transition, and the subscripts 1 and 2 indicate the values of buoyancy and buoyancy flux before and after the transition.

3. Scaling considerations

We normalize (1) to (5) using $V = V_g$ as the velocity scale and the planetary boundary layer depth H, interpreted as the distance from the slope over which the flow reaches a geostrophic equilibrium with buoyancy going to zero, as the length scale. This provides HV^{-1} for the time scale, V^2H^{-1} for the buoyancy scale, and V^2 for the normalized pressure scale, and yields the following normalized (scaled) governing equations:

$$\frac{\partial u_n}{\partial t_n} + u_n\frac{\partial u_n}{\partial x_n} + v_n\frac{\partial u_n}{\partial y_n} + w_n\frac{\partial u_n}{\partial z_n} = -\frac{\partial \pi_n}{\partial x_n} + \mathrm{Ro}^{-1}(v_n - 1) - b_n\sin\alpha + \mathrm{Re}^{-1}\left(\frac{\partial^2 u_n}{\partial x_n^2} + \frac{\partial^2 u_n}{\partial y_n^2} + \frac{\partial^2 u_n}{\partial z_n^2}\right), \tag{6}$$

$$\frac{\partial v_n}{\partial t_n} + u_n\frac{\partial v_n}{\partial x_n} + v_n\frac{\partial v_n}{\partial y} + w_n\frac{\partial v_n}{\partial z_n} = -\frac{\partial \pi_n}{\partial y_n} - \mathrm{Ro}^{-1}u_n + \mathrm{Re}^{-1}\left(\frac{\partial^2 v_n}{\partial x_n^2} + \frac{\partial^2 v_n}{\partial y_n^2} + \frac{\partial^2 v_n}{\partial z_n^2}\right), \tag{7}$$

$$\frac{\partial w_n}{\partial t_n} + u_n\frac{\partial w_n}{\partial x_n} + v_n\frac{\partial w_n}{\partial y_n} + w_n\frac{\partial w_n}{\partial z_n} = -\frac{\partial \pi_n}{\partial z_n} + b_n\cos\alpha + \mathrm{Re}^{-1}\left(\frac{\partial^2 w_n}{\partial x_n^2} + \frac{\partial^2 w_n}{\partial y_n^2} + \frac{\partial^2 w_n}{\partial z_n^2}\right), \tag{8}$$

$$\frac{\partial b_n}{\partial t_n} + u_n\frac{\partial b_n}{\partial x_n} + v_n\frac{\partial b_n}{\partial y_n} + w_n\frac{\partial b_n}{\partial z_n} = \mathrm{Bu}\times\mathrm{Ro}^{-2}(u_n\sin\alpha - w_n\cos\alpha) + \mathrm{Re}^{-1}\left(\frac{\partial^2 b_n}{\partial x_n^2} + \frac{\partial^2 b_n}{\partial y_n^2} + \frac{\partial^2 b_n}{\partial z_n^2}\right), \tag{9}$$

$$\frac{\partial u_n}{\partial x_n}+\frac{\partial v_n}{\partial y_n}+\frac{\partial w_n}{\partial z_n}=0, \tag{10}$$

where the subscript n denotes the normalized variables, $\mathrm{Ro}=HV^{-1}f^{-1}$ is the Rossby number, $\mathrm{Re}=VH\nu^{-1}$ is the Reynolds number, and $\mathrm{Bu}=N^2f^{-2}$ is the Burger number; the dimensionless product $\mathrm{Bu}\times\mathrm{Ro}^{-2}=N^2H^2V^{-2}$ may be considered as a Richardson number based on N.

The normalized boundary conditions for velocity and buoyancy on the slope (at $z_n=0$) are $u_n(0)=v_n(0)=w_n(0)$ and $b_n(0)=b_{sn}=b_sHV^{-2}\equiv-\mathrm{Ri}_b$, where Ri_b is the Richardson number based on the surface buoyancy, or $\partial b_n/\partial z_n(0)=-B_sH^2V^{-2}\nu_h^{-1}=-\mathrm{Ri}_B\mathrm{Re}$, where $\mathrm{Ri}_B\equiv B_sHV^{-3}$ is the Richardson number based on the surface buoyancy flux (both these Richardson numbers vary with t_n in a prescribed manner). Away from the slope, at sufficiently large z_n, the normalized velocity and buoyancy fields satisfy the following conditions: $\partial u_n/\partial z_n=\partial v_n/\partial z_n=\partial b_n/\partial z_n=w_n=0$. The governing parameters of the normalized problem are thus α, Ro, Re, Bu, and either $\mathrm{Ri}_b(t_n)$ or $\mathrm{Ri}_B(t_n)$.

Assuming typical atmospheric values of scales and external parameters, namely $V=10\,\mathrm{m\,s^{-1}}$, $H=10^3\,\mathrm{m}$, $f=10^{-4}\,\mathrm{s^{-1}}$, $N=10^{-2}\,\mathrm{s^{-1}}$, $\nu=\nu_h=10^{-5}\,\mathrm{m^2\,s^{-1}}$, $|b_s|=0.1\,\mathrm{m\,s^{-2}}$, and $|B_s|=10^{-3}\,\mathrm{m^2\,s^{-3}}$, we obtain $\mathrm{Ro}=10^2$, $\mathrm{Re}=10^9$, $\mathrm{Bu}=10^4$, $|\mathrm{Ri}_b|=1$, and $|\mathrm{Ri}_B|=10^{-3}$. DNS of such high-Re flow would be practically impossible with currently available computer resources, so we need to identify ways to bring Re down to computationally tractable values on the order of 10^4 (Fedorovich and Shapiro 2009a). As one option, we may consider rescaling the simulated flow to dimensions representative of a laboratory experiment (LE). Taking, for example, $V=0.1\,\mathrm{m\,s^{-1}}$, $H=0.1\,\mathrm{m}$, $f=10^{-2}\,\mathrm{s^{-1}}$, $N=1\,\mathrm{s^{-1}}$, $\nu=10^{-6}\,\mathrm{m^2\,s^{-1}}$, $|b_s|=0.1\,\mathrm{m\,s^{-2}}$, and $|B_s|=10^{-5}\,\mathrm{m^2\,s^{-3}}$ (we call this the LE parameter set) provides $\mathrm{Ro}=10^2$, $\mathrm{Re}=10^4$, $\mathrm{Bu}=10^4$, $|\mathrm{Ri}_b|=1$, and $|\mathrm{Ri}_B|=10^{-3}$. In this case, the simulated flow is a downscaled analog of the atmospheric boundary layer with reproduced scales of motion extending from the large scale $\sim H=0.1\,\mathrm{m}$ down to the Kolmogorov (micro) scale $\eta\sim(\nu V^{-3}H)\sim10^{-4}\,\mathrm{m}$ [assuming $H/\eta\sim\mathrm{Re}^{3/4}$ after Pope (2000)].

Another option would be to consider a flow with typical atmospheric scales but to use a fluid with viscosity orders of magnitude larger than the viscosity of air. Adopting, accordingly, $V=10\,\mathrm{m\,s^{-1}}$, $H=10^3\,\mathrm{m}$, $f=10^{-4}\,\mathrm{s^{-1}}$, $N=10^{-2}\,\mathrm{s^{-1}}$, $\nu=10^{-6}\,\mathrm{m^2}$, $|b_s|=0.1\,\mathrm{m\,s^{-2}}$, and $|B_s|=10^{-3}\,\mathrm{m^2\,s^{-3}}$ [we call this the viscous atmosphere (VA) parameter set] yields $\mathrm{Ro}=10^2$, $\mathrm{Re}=10^4$, $\mathrm{Bu}=10^4$, $|\mathrm{Ri}_b|=1$, and $|\mathrm{Ri}_B|=10^{-3}$, which are equal to their LE-flow counterparts. Such equality of flow numbers between the small-scale LE flow and the large-scale VA flow signifies the dynamical similarity of these flows in terms of dimensionless solutions of (6)–(10) for the same value of slope angle α. In the VA simulation, we therefore reproduce flow motions in the range from the large (outer) scale $\sim H=10^3\,\mathrm{m}$ down to the small (inner) scale $\eta\sim(\nu^3V^{-3}H)^{1/4}\sim1\,\mathrm{m}$.

Note that DNS of the VA flow using governing equations in the dimensional (nonnormalized) form may be conceptually interpreted as large-eddy simulation (LES) of this flow employing the simplest possible subgrid turbulence model with constant subgrid eddy diffusivities for momentum and heat/buoyancy. We realize, though, that the more advanced subgrid closures, like the commonly employed Smagorinsky (1963) closure, would provide turbulent velocity fields that are more diffusive on small scales and more sustainable with respect to laminarization. Also, as noted in, for example, Williams et al. (2017), the onset of laminarization at given degree of hydrostatic stability is expected to be a function of Re.

4. Numerical simulation

a. Simulation procedure and setup

The governing flow Eqs. (1)–(5) were spatially discretized and solved numerically in a domain of dimensions L_x, L_y, and L_z in the x, y, and z directions, respectively. The solution was carried out by a numerical algorithm with a fourth-order finite differencing of advection and diffusion terms in the transport equations, and with the fourth-order Runge–Kutta scheme applied for the time integration (Van Heerwaarden et al. 2017). For the pressure, a fourth-order Poisson solver was used.

Initially, u, w, and b were set to zero in the zero-buoyant geostrophic flow (state of rest was also an option) with $v=V_g$ everywhere in the domain. Within the first time step, the boundary conditions for the velocity components and buoyancy at the bottom and top of the domain were implemented. Additionally, the buoyancy was randomly perturbed over the (x, y) plane at the first numerical z level above the slope. The purpose of this randomization of the near-surface buoyancy field was to facilitate the transition to turbulence during the daytime phase of the simulation, when $b_{s1}>0$ and $B_{s1}>0$, depending on the type of the buoyancy boundary condition at $z=0$.

In each simulation, a slope-following (tilted) daytime convective boundary layer (CBL) was driven by either a positive surface buoyancy or buoyancy flux. In the presence of the southerly geostrophic wind, and under the combined effect of the upslope (anabatic) buoyant acceleration and the Coriolis force, the CBL progressively

grew in thickness and developed an upslope flow component. At some point in the CBL mature phase, the surface buoyancy (or buoyancy flux) was dropped to a lower (always negative in the flux case) nighttime value. The response of the boundary layer flow to this change in surface forcing was occurring as an oscillation that had both gravitational (as reaction to the weaker buoyancy forcing) and inertial (associated with weakened near-surface friction) components.

For the presentation of results, all setup parameters and simulation variables were rescaled to the VA dimensions. All presented flow variables are obtained by spatial averaging over the terrain-parallel planes.

b. *Summary of simulated flow cases and grid sensitivity tests*

Nineteen simulations (denoted as B simulations) were conducted with the buoyancy prescribed as the surface forcing. In these simulations, the sensitivities of the simulated jets to slope angle, grid configuration, and geostrophic wind magnitude were investigated. Each B simulation was run for 54 000 s (15 h) with the first 10 800 s (3 h) allocated for the daytime CBL development. The daytime surface buoyancy b_{s1} in these simulations was set to $0.1\,\mathrm{m\,s^{-2}}$. The grid cell size Δ was spatially uniform and equal to 4 m. The diffusivity $\nu = \nu_h$ was set to $1\,\mathrm{m^2\,s^{-1}}$ and N to $10^{-2}\,\mathrm{s^{-1}}$. The setup parameters for individual B simulations are listed in Table 1.

Another 19 simulations (denoted as F simulations) were conducted with the buoyancy flux prescribed as the surface forcing. Like the B simulations, each F simulation was run for 54 000 s, with the first 10 800 s being allocated for the daytime CBL development. The daytime surface buoyancy flux B_{s1} in the F simulations was set to $3 \times 10^{-3}\,\mathrm{m\,s^{-2}}$. The grid cell size Δ (4 m), $\nu = \nu_h$ ($1\,\mathrm{m^2\,s^{-1}}$), and frequency N ($10^{-2}\,\mathrm{s^{-1}}$) values were the same as in the B simulations. The setup parameters for individual F simulations are listed in Table 2.

A stand-alone numerical experiment (denoted as simulation Z) was designed to investigate the formation of the Great Plains nocturnal LLJ in the absence of external geostrophic forcing. This simulation was run for 54 000 s with a prescribed buoyancy as the surface forcing, with the following parameter settings: daytime duration 10 800 s, daytime surface buoyancy $b_{s1} = 0.4\,\mathrm{m\,s^{-2}}$, nighttime surface buoyancy $B_{s2} = 0$, $\alpha = 0.18°$, $V_g = 0$, $\nu = \nu_h = 1\,\mathrm{m^2\,s^{-1}}$, and $N = 2 \times 10^{-2}\,\mathrm{s^{-1}}$. A numerical grid with $N_x \times N_y \times N_z = 256 \times 256 \times 384$ nodes was employed, with a uniform spacing of $\Delta = 4$ m.

A separate set of simulations (denoted as G simulations) was run to test the sensitivity of the simulated flow fields to the overall size of the numerical grid and its spacing. Each G simulation was conducted for 24 000 s with a prescribed surface buoyancy b_s value of $0.2\,\mathrm{m\,s^{-2}}$ during the first 3600 s (1 h) and $-0.025\,\mathrm{m\,s^{-2}}$ for the remaining time. For all G simulations: $\alpha = 0.18°$, $V_g = 5\,\mathrm{m\,s^{-1}}$, $\nu = \nu_h = 1\,\mathrm{m^2\,s^{-1}}$, and $N = 10^{-2}\,\mathrm{s^{-1}}$. The setup parameters for the individual G simulations are presented in Table 3, and the corresponding test results are shown in Fig. 3. Individual plots in this figure present the evolving wind speed profiles obtained with six different numerical grid configurations. During the daytime, the wind field is vertically well mixed in the established CBL, with the wind being subgeostrophic throughout the mixed region. After the transition to the nighttime, the wind field gradually adjusts to the less turbulent nocturnal conditions, forming the low-level jet with a maximum wind speed at about 350 m above ground level (AGL). Simulations with all grid settings agree well in predicting both this level and the corresponding wind magnitude. Normalized wind profiles from the different G simulations indicate that with regards to wind speed the outputs of G3, G5, and G6 simulations are sufficiently close to each other to justify the use of G3's $256 \times 256 \times 384$ grid with $\Delta = 4$ m as the default grid configuration for our numerical experiments. This grid configuration appears to be optimal in terms of the balance between accuracy of representing velocity fields and computational efficiency. Some simulations listed in Tables 1 and 2 were conducted on larger grids in order to

TABLE 1. Setup parameters for the B simulations (buoyancy as the lower boundary condition). Here, N_φ is the number of grid cells along the L_φ dimension, b_{s2} ($\mathrm{m\,s^{-2}}$) is the nighttime (post-sunset) surface buoyancy, V_g is the geostrophic wind magnitude ($\mathrm{m\,s^{-1}}$), and α is the slope angle (°). The daytime surface buoyancy b_{s1} in all B simulations was $0.1\,\mathrm{m\,s^{-2}}$.

Simulation	b_{s2}	V_g	α	$N_x \times N_y \times N_z$
B1	−0.02	5	0.18	512 × 512 × 384
B2	−0.05	5	0.18	512 × 512 × 384
B3	0.00	5	0.18	256 × 256 × 384
B4	0.03	10	0.18	256 × 256 × 384
B5	0.03	10	0.18	512 × 512 × 384
B6	0.03	20	0.18	256 × 256 × 384
B7	0.05	5	0.00	256 × 256 × 384
B8	0.05	5	0.18	256 × 256 × 384
B9	0.05	5	0.00	512 × 512 × 384
B10	0.05	5	0.18	512 × 512 × 384
B11	0.05	10	0.00	256 × 256 × 384
B12	0.05	10	0.09	256 × 256 × 384
B13	0.05	10	0.18	256 × 256 × 384
B14	0.05	10	0.27	256 × 256 × 384
B15	0.05	10	0.00	512 × 512 × 384
B16	0.05	10	0.18	512 × 512 × 384
B17	0.06	5	0.18	512 × 512 × 384
B18	0.07	5	0.18	512 × 512 × 384
B19	0.07	10	0.18	512 × 512 × 384

TABLE 2. Setup parameters for the F simulations (buoyancy flux as the lower boundary condition). Here, B_{s2} ($m^2 s^{-3}$) is the nighttime (post sunset) surface buoyancy flux. The daytime surface buoyancy flux B_{s1} in all F simulations was $3 \times 10^{-3}\,m\,s^{-2}$. The remaining notation is as in Table 1.

Simulation	B_{s2}	V_g	α	$N_x \times N_y \times N_z$
F1	0	10	0.18	$256 \times 256 \times 384$
F2	-3.00×10^{-5}	10	0.18	$256 \times 256 \times 384$
F3	-3.00×10^{-5}	20	0.18	$256 \times 256 \times 384$
F4	-1.50×10^{-4}	10	0.18	$256 \times 256 \times 384$
F5	-1.50×10^{-4}	20	0.18	$256 \times 256 \times 384$
F6	-3.00×10^{-4}	10	0.18	$256 \times 256 \times 384$
F7	-3.00×10^{-4}	20	0.18	$256 \times 256 \times 384$
F8	-6.00×10^{-4}	20	0.18	$256 \times 256 \times 384$
F9	-7.20×10^{-4}	20	0.00	$256 \times 256 \times 384$
F10	-7.20×10^{-4}	20	0.09	$256 \times 256 \times 384$
F11	-7.20×10^{-4}	20	0.18	$256 \times 256 \times 384$
F12	-7.20×10^{-4}	20	0.27	$256 \times 256 \times 384$
F13	-7.20×10^{-4}	20	0.18	$512 \times 512 \times 384$
F14	-7.35×10^{-4}	20	0.18	$256 \times 256 \times 384$
F15	-7.50×10^{-4}	20	0.00	$256 \times 256 \times 384$
F16	-7.50×10^{-4}	20	0.18	$256 \times 256 \times 384$
F17	-7.50×10^{-4}	20	0.18	$512 \times 512 \times 384$
F18	-9.00×10^{-3}	20	0.18	$256 \times 256 \times 384$
F19	-1.50×10^{-3}	20	0.18	$256 \times 256 \times 384$

TABLE 3. Numerical grid parameters in test simulations with different grid configurations (G simulations), where Δ (m) is the directionally uniform grid spacing and N_φ is defined as in Table 1.

Simulation	Δ	$N_x \times N_y \times N_z$
G1	4	$128 \times 128 \times 384$
G2	2	$256 \times 256 \times 768$
G3	4	$256 \times 256 \times 384$
G4	2	$512 \times 512 \times 768$
G5	4	$512 \times 512 \times 384$
G6	2	$1024 \times 1024 \times 768$

further investigate the grid-size effects on the simulated flow fields.

5. Analyses of simulated flow regimes

We will group our main findings from the B and F simulations according to the particular features of the LLJ structure and evolution, and analyze different simulated LLJ flow regimes in association with these features. For the B simulations, it was found that a relatively strong geostrophic wind ($10\,m\,s^{-1}$ or stronger) was required to maintain some level of turbulence in the LLJ flow during the night. Turbulence within the boundary layer had a general tendency to fade during the night when the nighttime surface buoyancy b_{s2} was less than half of the daytime surface buoyancy b_{s1}, except for case B6, in which the nighttime turbulence survived owing to the $20\,m\,s^{-1}$ geostrophic wind. On the other hand, the simulated LLJ in case B19 was very weak due to the quite intense nighttime turbulence associated with the relatively strong geostrophic wind and large surface buoyancy, which essentially incapacitated the inertial branch of the jet-formation mechanism. As will be discussed in section 5b, the above-slope buoyancy weakens during the night due to along-slope advection of the environmental potential temperature and can lead to the destabilization of the practically laminar LLJ flow and to the reemergence of turbulence. Overall, marked differences in jet evolution and structure were found among the B cases. These different features will be considered in more detail in the subsequent sections of the paper.

Also in the F simulations, a geostrophic wind stronger than $10\,m\,s^{-1}$ was generally required to maintain detectable turbulence levels during the nighttime. For a given V_g, a slight variation of the nighttime surface buoyancy flux around some threshold value had a drastic effect on turbulence levels in the nocturnal boundary layer. For instance, cases F11 and F16, which differ very slightly with respect to B_{s2}, produced nighttime LLJs with very different turbulence properties: in the case with the smaller magnitude of negative B_{s2} (F11), the turbulence level in the boundary layer was merely reduced throughout the night compared to the daytime conditions, while in case F16 (larger magnitude of B_{s2}), the turbulence was essentially shut down over the main portion of the night. Accordingly, there were drastic differences in the LLJ velocity profile and its evolution between these two cases. The reemergence of turbulence during the night, mentioned above in connection with the B simulations, was also occasionally observed in the F simulations, but was not that common. A relatively strong dependence of LLJ evolution patterns on slope angle and grid configuration observed in the B simulations, was also found in the F simulations.

Inspection of results from the B and F simulations point to the existence of two major LLJ regimes that are distinguished by the levels of turbulence exhibited in the evolving nocturnal boundary layer flow. The first regime, which we will refer to as the quiet-night (QN) regime, is characterized by the almost complete decay of turbulence over a relatively short time (about 1 h) after sunset. The second regime, hereafter called the turbulent-night (TN) regime, features significant levels of turbulence maintained either continuously throughout the entire night or over a major portion of it, including cases of nocturnal turbulence reemergence.

a. LLJ structure and evolution in the QN regime

The height–time evolution of the turbulence kinetic energy (TKE) for two simulated QN cases of the LLJs

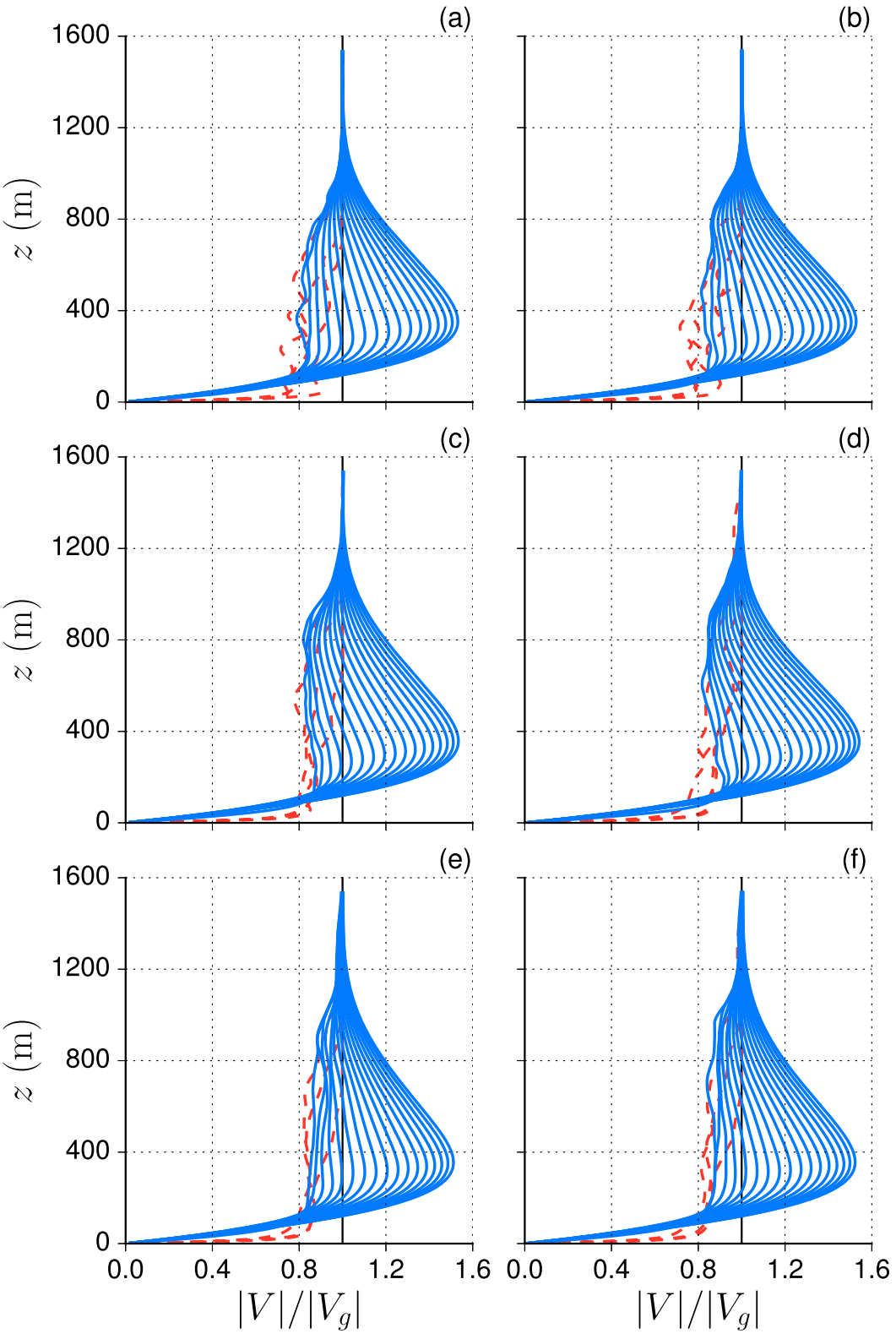

FIG. 3. Evolution of the normalized wind speed $|V|/|V_g|$ where $|V| = (u^2 + v^2)^{1/2}$ in the simulations with different grid settings (Table 3): (a) G1, (b) G2, (c) G3, (d) G4, (e) G5, and (f) G6. Individual profiles are shown with a time interval of 1200 s. Three daytime profiles are indicated by dashed red lines, and nocturnal (post-sunset) profiles by solid blue lines.

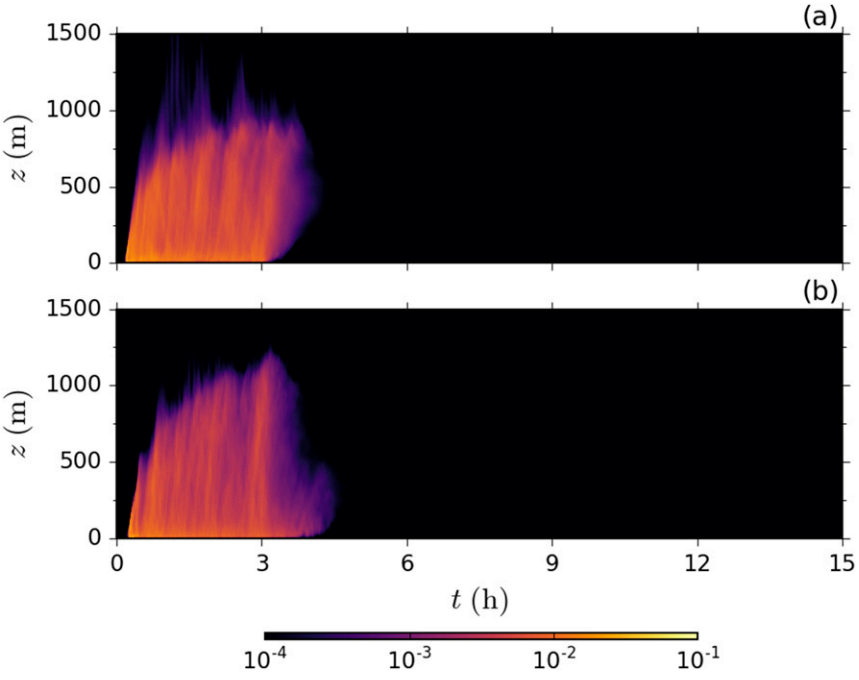

FIG. 4. Height–time distribution of the normalized turbulence kinetic energy TKE/$|V_g|^2$ in two simulated LLJs of the QN type: (a) B4 and (b) F16.

developing in response to the drops in the surface buoyancy (case B4) and surface buoyancy flux (case F16) is illustrated in Fig. 4. The TKE was evaluated as

$$\mathrm{TKE} = \frac{1}{2}(\overline{u'^2} + \overline{v'^2} + \overline{w'^2}), \tag{11}$$

where the overbars signify the averaging, while the primes denote deviations of the corresponding velocity components from their average values. In both cases, vigorous turbulence develops during the daytime (at t less than 3 h), followed be a relatively fast decay of turbulence within post-sunset transition periods. This decay happens quite differently in the two considered cases. In case B4, the turbulence decouples from the surface almost immediately and weakens from the bottom upward, while in case F16, it survives for some time, especially in the near-surface region of the flow, before being essentially shut down by an increased static stability. Overall, the turbulence decay occurs on the time scale of an hour in case B4 and on the scale of an hour and a half in case F16. In the latter case, the stronger geostrophic wind and associated stronger shear apparently contribute to the enhanced turbulence longevity. The turbulence remains extremely weak throughout the rest of the night in both cases.

A more detailed picture of the structural and quantitative changes in turbulence during the day-to-night transition in cases B4 and F16 is presented in Fig. 5. Here we show horizontal cross-sections of u, v, w, and potential temperature deviation $\theta = \Theta - \Theta_r$ introduced as

$$\theta = \frac{\Theta_r}{g}[b - N^2(L_z - z)], \tag{12}$$

with Θ_r set to 300 K. In (12) we neglected the very slight difference (due to the smallness of α) between the distance along the slope-normal coordinate z and the actual vertical coordinate z'. Note that because of the presence of stronger geostrophic wind (and associated stronger flow shear), turbulent velocity fluctuations have larger magnitudes in case F16 than in case B4. The stronger shear in case F16 also leads to more energy being carried by smaller-scale turbulence motions toward the end of transition as compared to case B4. This effect may be clearly seen by contrasting the w patterns for cases B4 and F16 at the same times. The spatial variability of the decaying θ fluctuations shows a similar trend toward smaller scales. In both cases, the decaying turbulence becomes progressively less organized with time. Roll-like convective structures that are dominant in the flow at sunset give way to much more chaotic flow structures as the turbulence decays throughout the transition period.

Evolving nighttime profiles of buoyancy, potential temperature deviation, and the velocity components in

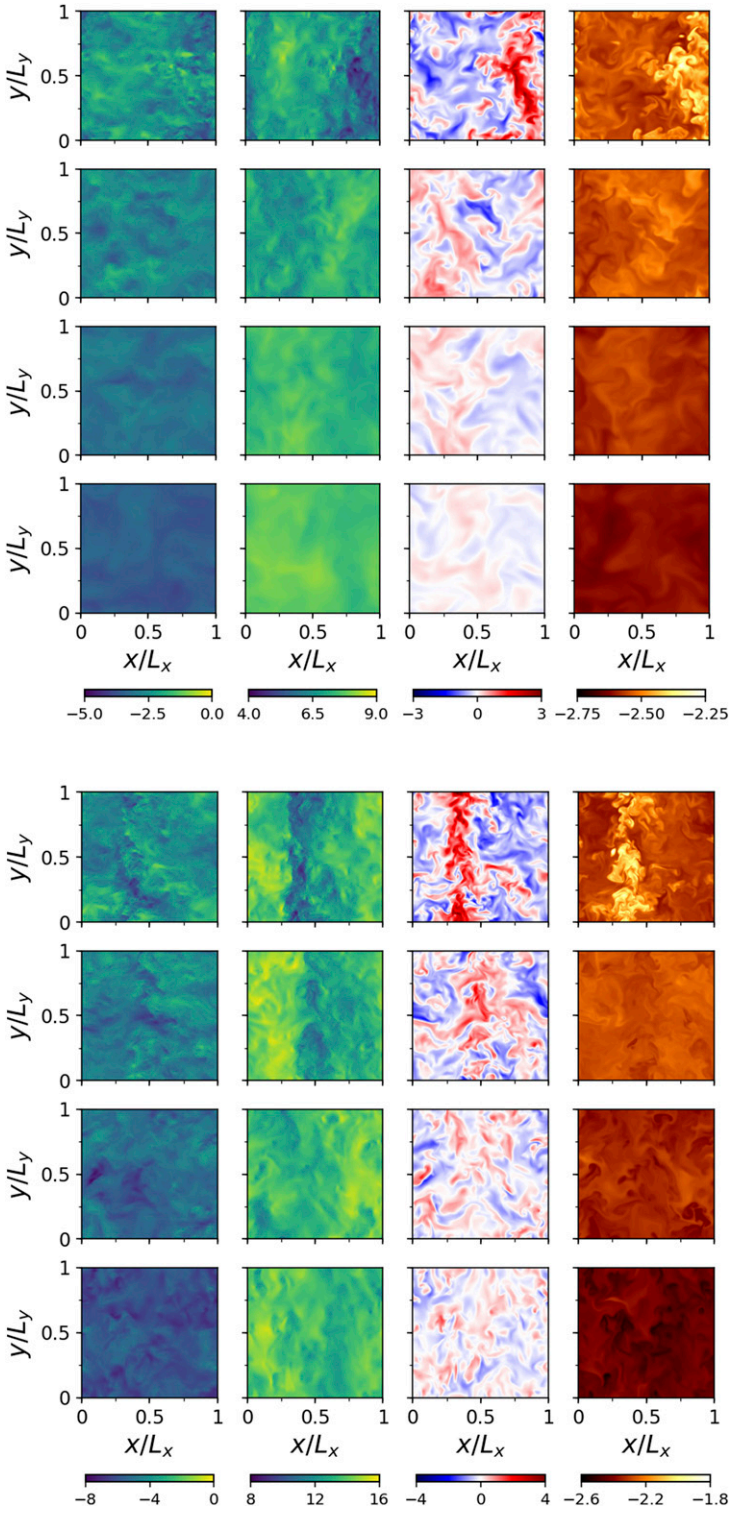

FIG. 5. Evolution of normalized turbulent flow fields over x–y planes at 350 m AGL in the post-sunset phases of two QN LLJ simulations: (top) B4 and (bottom) F16: (left to right) u, v, w (all m s^{-1}), and θ (K); (top to bottom in each part): t = 180 (sunset), 200, 220, and 240 min.

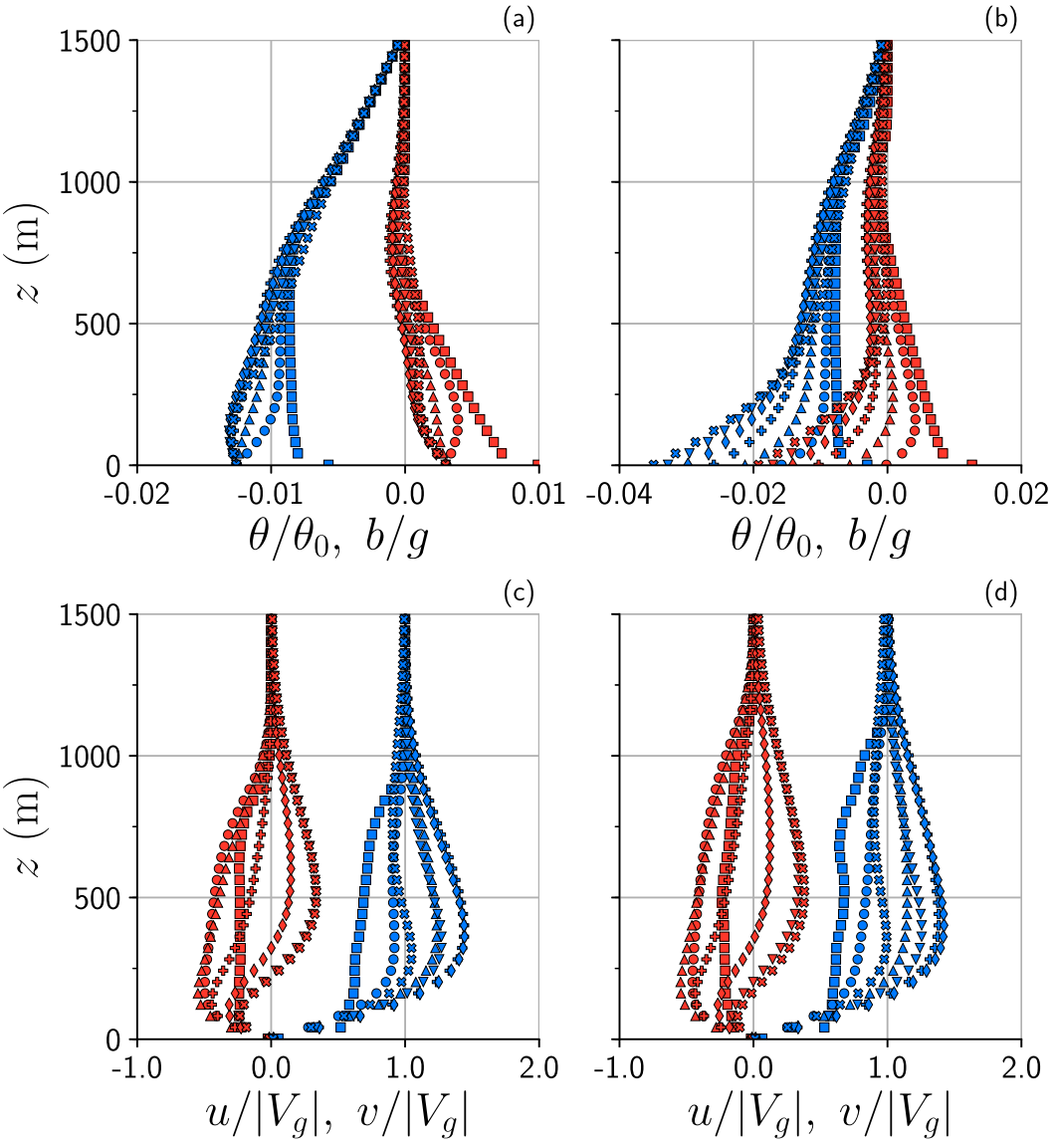

FIG. 6. Normalized profiles of (a),(b) b (red) and potential temperature deviation θ (blue) and (c),(d) u (red) and v (blue) in two QN LLJs, from the (left) B4 and (right) F16 simulations. Squares show profiles at $t = 10\,800$ s (sunset), circles = 18 000 s (2 h into the night), triangles = 25 200 s, plus signs = 32 400 s, diamonds = 39 600 s, inverted triangles = 46 800 s, and crosses = 54 000 s (12 h into the night).

the QN regime are shown in Fig. 6. The buoyancy in the plots is normalized by the gravity acceleration $g = 9.8\,\mathrm{m\,s^{-2}}$, and the potential temperature deviation by $\theta_0 = \Theta_r$. The b and θ profiles at sunset ($t = 3$ h), before the drop in the surface buoyancy forcing, are qualitatively similar for cases B4 and F16 (Figs. 6a and 6b, respectively): the buoyancy linearly decreases with height throughout the mixed layer, the region of essentially height-constant potential temperature. However, after the onset of the nighttime surface forcing, b and θ evolve rather differently between the two cases.

In case B4 (Fig. 6a), the buoyancy at the surface remains constant, while the buoyancy above the slope, within the residual layer that is the remnant of the previously existing mixed layer, gradually decreases with time. As can be readily concluded from the change of the buoyancy profile in Fig. 6a and the observed u component (Fig. 6c), this decrease is primarily caused by the negative buoyancy production $N^2 u \sin\alpha$ [see Eq. (4)] associated with advection of the environmental potential temperature up the slope. The upslope advection has its maximum magnitude at about 200 m above the slope,

where the rate of the buoyancy change in time is the highest. The resulting temporal decrease of the potential temperature above the slope is strongly height dependent. Because θ remains constant at the slope but decreases in the fastest manner at the 200-m height, there is a reduction of the vertical gradient of the potential temperature below 200 m and thus a diminishing of the static stability above the slope. The decrease of stability does not reach the critical point in this case, and the flow remains quiescent overall (see Fig. 4). However, under other conditions, as we will see later in the case of the TN flow (section 5b), the upslope advection of Θ_e can lead to the destabilization of the lower portion of the LLJ flow and a reemergence of strong turbulence.

The velocity-component profiles in Fig. 6c, corresponding to the buoyancy and temperature profiles in Fig. 6a, illustrate the development of the nocturnal LLJ from an initially well-mixed southeasterly flow. Note that a significant upslope flow ($u < 0$) develops during the day under the joint effect of negative contributions from $f(v - V_g)$ [inertial term in Eq. (1)] and $-b\sin\alpha$ [gravity term in Eq. (1)]. Profiles of both u and v components at sunset ($t = 3$ h) reveal zones of the near-surface and elevated shears (the latter being roughly collocated with the entrainment zone at the top of convectively mixed layer evident in the corresponding b and θ profiles). In response to the cessation of the surface buoyancy at $t = 3$ h and the subsequent reduction of the frictional constraint, jetlike features develop in the velocity component profiles rather rapidly, roughly within four hours after transition into the night. The LLJ achieves its maximum magnitude ~7 h after sunset, with peak wind speeds exceeding $1.5|V_g|$. Toward the end of the night, the u velocity profile attains a characteristic shape with a narrow near-surface negative minimum and an elevated broad positive maximum. The latter feature points to the downslope transport of Θ_e within the upper branch of the LLJ leading to the buoyancy increase in this flow region.

In case F16 (Fig. 6b), it is the vertical gradient of buoyancy (proportional to the buoyancy flux) at the slope that remains constant throughout the night. This positive buoyancy gradient corresponds to a positive vertical gradient of θ close to the surface, which remains positive [see Eq. (12)] and constant during the night. Therefore, in the presence of upslope advection of Θ_e analogous to the one that occurred in case B4, the potential temperature at the surface just slides in time toward lower values while retaining stable stratification in the near-surface flow region. In terms of the θ gradient, the stratification remains stable within the entire residual layer. Toward the end of the night, a strong downslope flow component develops within the 300- to 1000-m layer due to the inertial oscillation (Fig. 6d), and the buoyancy production $N^2 u\sin\alpha$ in this layer becomes positive, which leads to a steepening of the θ profile and an increase of the static stability.

Figure 7 illustrates the evolution of the QN LLJ in terms of the wind speed $|V| = (u^2 + v^2)^{1/2}$. The jet develops in a similar manner under conditions of the surface buoyancy (Fig. 7a) and buoyancy flux (Fig. 7b) forcing. In both cases, wind speed maxima throughout the night occur at the height of about 300 m AGL. During the early stages of jet development, there is a subtle descent of the wind maximum. However, when the jet becomes strong, the elevation of the wind maximum remains approximately constant. The corresponding wind hodographs, shown in Fig. 8, reveal two particular features of the simulated QN LLJs. The first feature is the essential noncircularity of the hodographs at all elevations. This feature points to a principal difference in the hodograph shape between the simulated LLJs and idealized jets with circular hodographs described by Blackadar (1957) and Van de Wiel et al. (2010). In this respect, the jet hodographs in Fig. 8 are much closer in shape to the hodographs predicted in the analytical study of Great Plains LLJs by Shapiro et al. (2016); see their Fig. 6. The second feature is the progressive growth with height of the positive (downslope) velocity component that has been discussed above in association with the velocity profiles in Figs. 6c and 6d. In the real nocturnal boundary layer over the Great Plains such elevated downslope transport could supply heat and moisture to regions eastward with a potential for convection initiation. In fact, a very similar evolution pattern of the flow velocity (Fig. 9) was observed during one of the intensive observation periods of the recent Plains Elevated Convection at Night (PECAN) experiment (Geerts et al. 2017) when convection was indeed observed later in the night. The observed velocity profiles show the same developmental tendencies as their simulated counterparts presented in Fig. 6.

b. *LLJ structure and evolution in the TN regime*

As in our analysis of the QN regime, we consider the evolution of the TKE in nocturnal boundary layers with LLJs driven by the surface buoyancy (B13; Fig. 10a) and surface buoyancy flux (F11; Fig. 10b) forcings. In both cases, significant levels of TKE are retained in the evolving LLJs either over the whole night or over a significant portion of it. In case B13, the TKE drops to very low values within an hour after sunset, only to violently reemerge a few hours later. With the buoyancy flux forcing (case F11), the TKE is greatly reduced after sunset but then gradually increases to about two-thirds of its daytime value. However, in this latter case, the

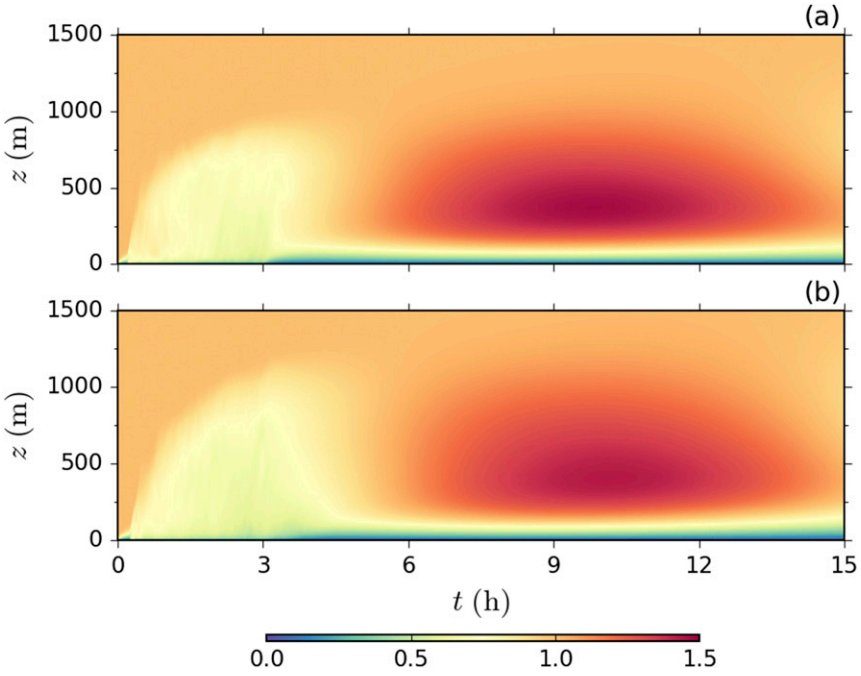

FIG. 7. Height–time distributions of the normalized wind speed $|V|/|V_g|$ in two QN LLJ simulations: (a) B4 and (b) F16.

restored turbulent mixed layer is noticeably shallower than the mixed layer during the day. It also undergoes further shrinking toward the end of the night. In both TN cases, we thus observe the generation of a new, relatively shallow turbulent layer in place of the completely or partially collapsed daytime convectively mixed layer.

The corresponding evolution of the b and θ profiles may be tracked in Figs. 11a and 11b. In case B13, the weaker shear associated with weaker geostrophic wind

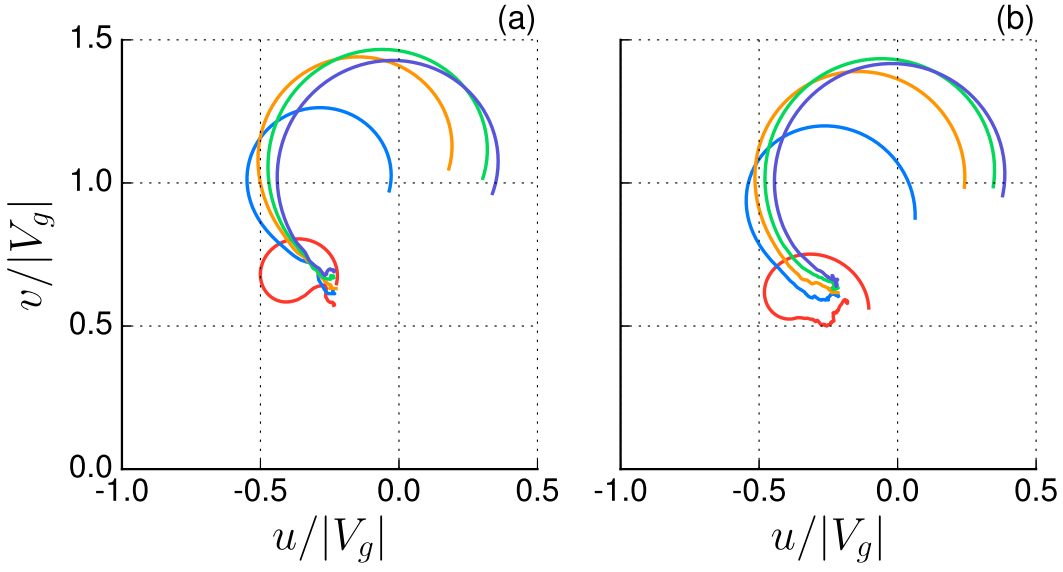

FIG. 8. Normalized wind hodographs from the (a) B4 and (b) F16 simulations of the QN LLJs. Different line colors correspond to different elevations AGL: 100 (red), 200 (blue), 300 (orange), 400 (green), and 500 m (purple). The hodographs cover the 12-h time periods from 3 h (sunset) to 15 h into the simulations.

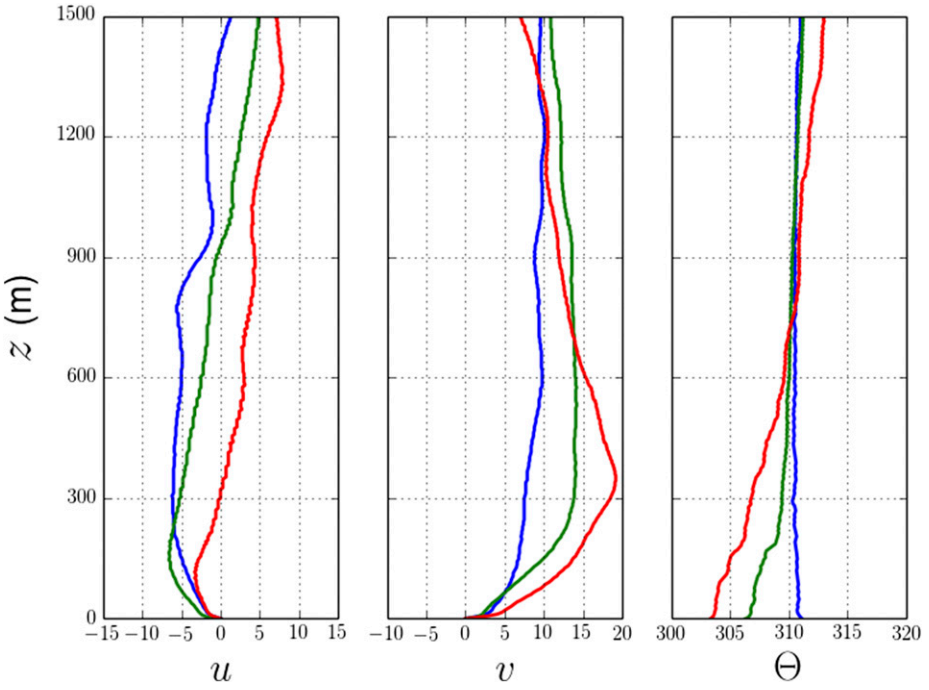

FIG. 9. (left to right) Profiles of u and v ($\mathrm{m\,s^{-1}}$) and potential temperature Θ (K) from the fixed PECAN Integrated Sounding Array 3 (FP3) in Ellis, Kansas, on 5 July 2015 at 0000 UTC (around time of sunset; blue), 0300 UTC (green), and 0600 UTC (red). Data source: Clark (2015).

coupled with a vertical gradient of θ comparable to that in case F11 indicates that flow conditions after sunset are more turbulence-suppressive than in case F11. This explains the practically complete shutdown of turbulence shortly after sunset in case B13 as compared to the mere reduction of TKE in case F11 (cf. Figs. 10a and 10b). However, because of the previously discussed gradual decrease of above-slope buoyancy associated with

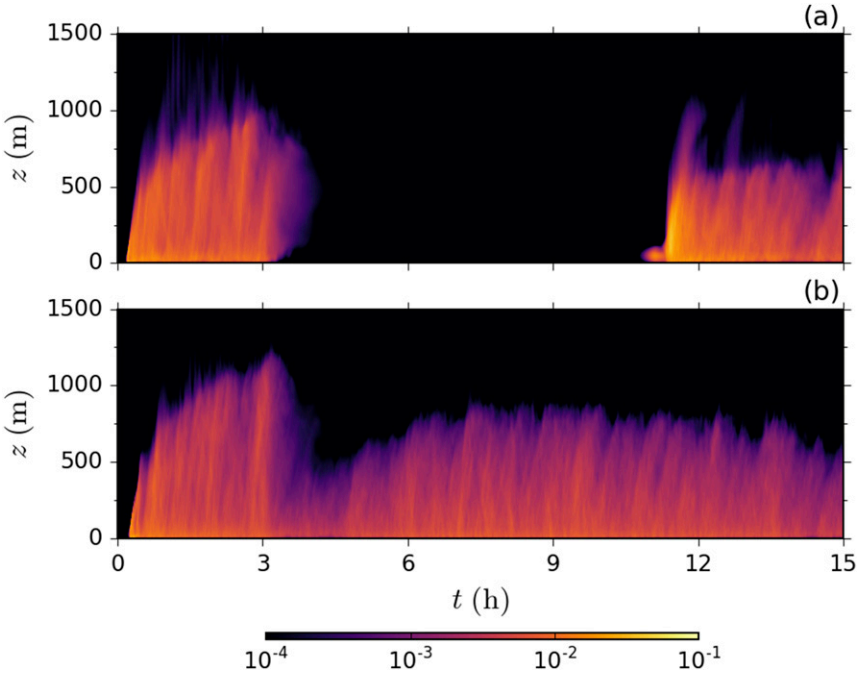

FIG. 10. Height–time distribution of the normalized turbulence kinetic energy TKE/$|V_g|^2$ in two simulated LLJs of the TN type: (a) B13 and (b) F11.

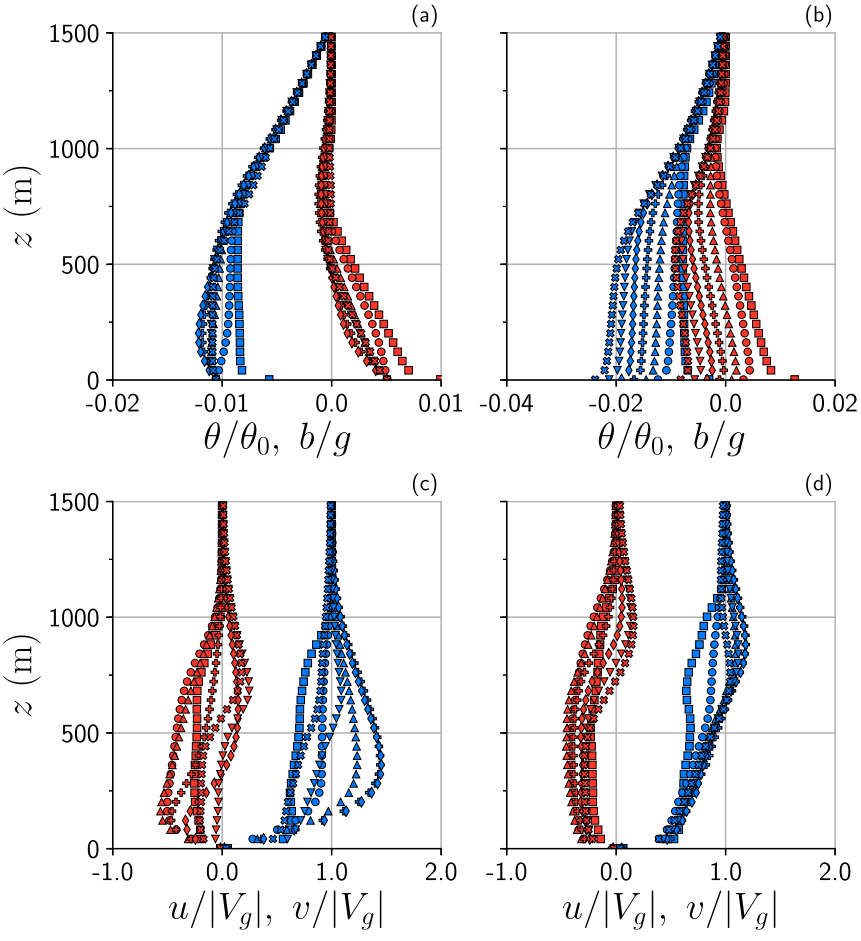

FIG. 11. As in Fig. 6, but for two TN LLJs, showing profiles from the (left) B13 and (right) F11 simulations. All symbols are as in Fig. 6.

advection of Θ_e, the near-surface potential temperature gradient in case B13 progressively weakens and at some point changes its sign, creating conditions for flow destabilization and the reemergence of the turbulence (Fig. 11a).

The b and θ evolution with surface buoyancy-flux forcing (case F11) is quite different (Fig. 11b). As a result of the buoyancy decrease due to the Θ_e advection, the b and θ profiles in this case just slide along the axis toward smaller values, with vertical gradients of the both fields remaining constant. The gradient of θ in the near-surface portion of the boundary layer after sunset remains slightly positive but relatively small, which is indicative of weakly stable conditions that apparently do not prohibit turbulence maintenance. Changes of the θ gradient with time in Fig. 11b qualitatively match the evolution pattern of the TKE field in Fig. 10b.

The corresponding variations of the velocity components in cases B13 and F11 are illustrated in Figs. 11c and 11d. In case B13 (Fig. 11c), the initial stages of the velocity evolution are similar to the corresponding wind profile changes in case B4 (Fig. 6c), where a pronounced LLJ develops by 39 600 s into simulation (7 h after sunset). However, between 39 600 s and 46 800 s (~8 h after sunset), as the jet started to weaken, the momentum gets mixed across the jet due to the destabilization caused by the Θ_e advection (see Fig. 11a). Such remixing rapidly destroys most of the original jet (note the abrupt wind speed change in Fig. 12a) and leaves behind a much weaker elevated jet at ~600 m; see velocity profiles referring to 46 800 s in Fig. 11c. As Fig. 12a indicates, this residual elevated jet gradually fades out toward the end of the night. Since turbulent mixing in case F11 never completely ceased during the night (Fig. 10b), the development of the LLJ in this case is strongly affected by the remaining vertical mixing of momentum in the lower portion of the boundary layer, while the release of the frictional constraint affects only the elevated portion of the flow. As a result, a weak elevated jet develops at 800 m AGL after sunset. Morphologically this jet is

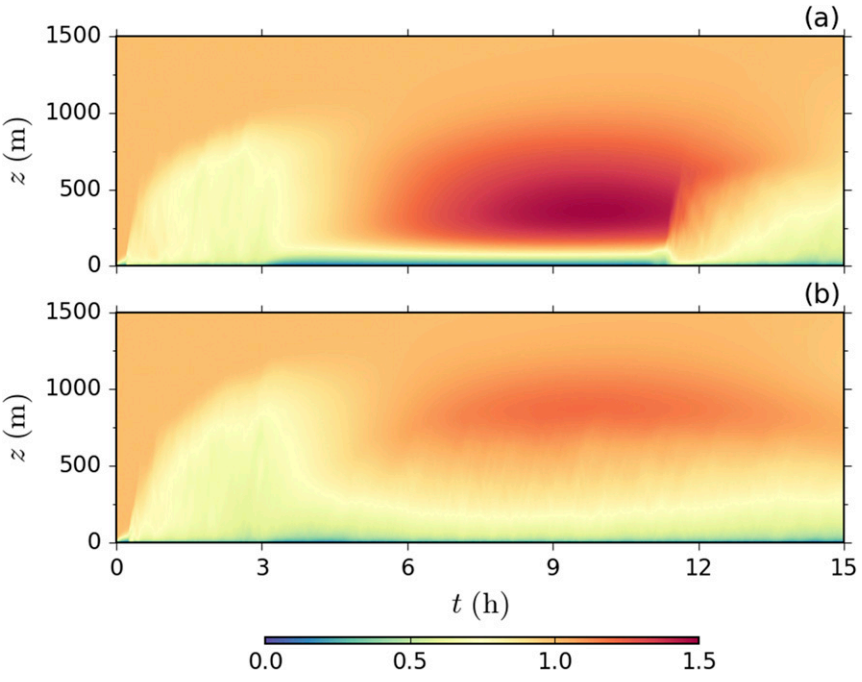

FIG. 12. As in Fig. 10, but of the normalized wind speed $|V|/|V_g|$.

similar to the jet that forms following the reemergence of turbulent mixing after 46 800 s in case B13 (Fig. 11c) but lasts longer, throughout the major portion of the night (Fig. 11d). This elevated TN jet is considerably weaker than its QN counterpart (Figs. 6d and 7b) and has a markedly different wind profile.

Because of the mixing and remixing of momentum in the TN jets, their hodographs (Fig. 13) are completely different from the hodographs of the QN jets (Fig. 8). In case B13, the reemergence of turbulence as result of the boundary layer remixing toward the end of the night erodes the jet previously formed within a 500-m-deep layer (Fig. 12a). This erosion is revealed in the figure by fractured and convoluted segments of the hodographs. In case F11 (Fig. 13b), the magnitudes of the velocity oscillations in the hodographs beneath 500 m are small

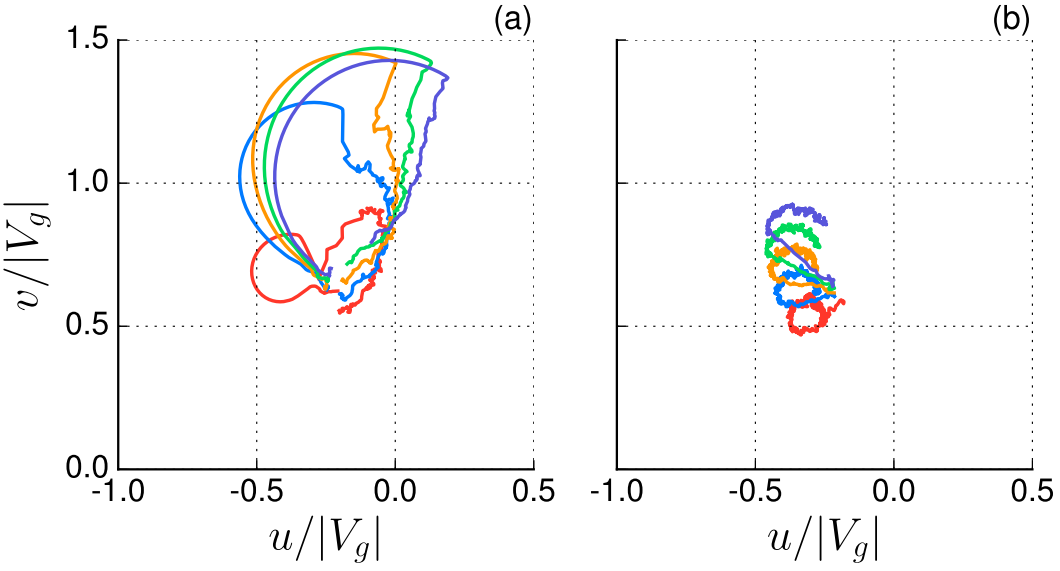

FIG. 13. As in fig. 8, but from (a) B13 and (b) F11 simulations of the TN LLJs.

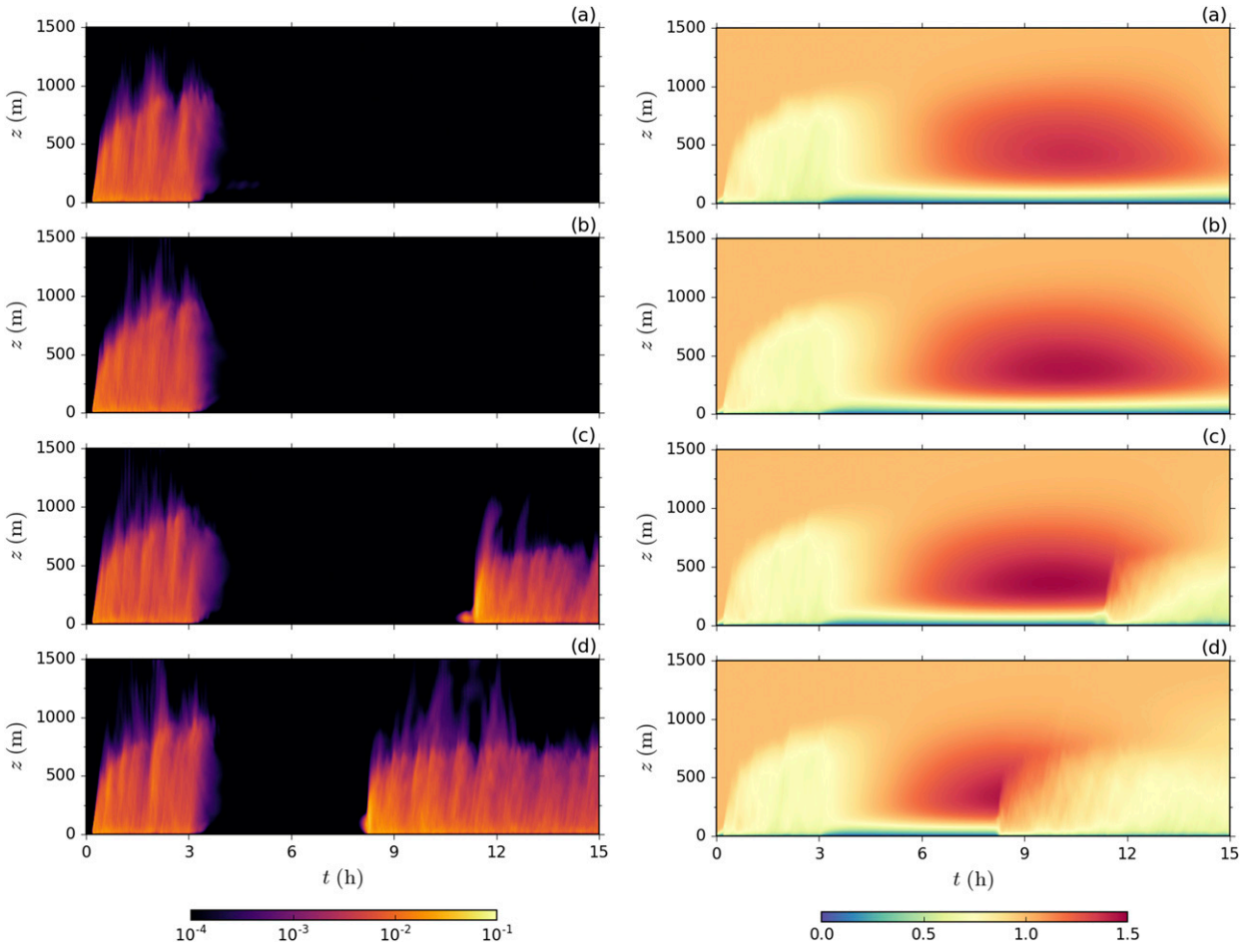

FIG. 14. Height–time distributions of the (left) normalized turbulence kinetic energy TKE/$|V_g|^2$ and (right) normalized wind speed $|V|/|V_g|$ from simulations with prescribed surface buoyancy: (a) B11 ($\alpha = 0°$), (b) B12 ($\alpha = 0.09°$), (c) B13 ($\alpha = 0.18°$), and (d) B14 ($\alpha = 0.27°$).

because of the reduced temporal variability of the wind profiles associated with the ongoing mixing.

c. *Effects of the slope*

We next consider the effects of the slope on the structure and evolution of southerly LLJs. As a reference, two LLJ cases over flat terrain were considered: a case with surface buoyancy forcing (B11) and a case with surface buoyancy-flux forcing (F9).

Results of experiments with the surface buoyancy forcing and varying slope angle α are summarized in Fig. 14. Apart from α, all setup parameters are kept the same. As Fig. 14 shows, LLJs develop in all cases, but their evolution and terminal state differ from case to case. With the shallowest slope of 0.09°, the formation of the jet and its evolution are very similar to those of the flat-terrain jet, but the wind maximum is slightly stronger. The stronger jet in the case of the slope may be explained by the contribution of buoyancy before sunset, which enhances the westward (upslope) pressure gradient force and results in a stronger inertial oscillation. Such jet amplification due to the shallow slope was predicted in theoretical analyses of Shapiro and Fedorovich (2009) and Shapiro et al. (2016). Either with or without a slope, jets exist throughout the entire night in the low-turbulent environment, so they both correspond to the QN regime. In the case of flat terrain, there is no along-slope advection of Θ_e, so flow destabilization due to this advection does not occur. Since the effect of the Θ_e advection is proportional to $\sin\alpha$, the associated buoyancy decrease with time in the lower region of the flow is very slow in the smallest angle case, and the stratification destabilization does not reach a tipping point. The flow thus remains very weakly turbulent, like in the case of the LLJ over the flat terrain. However, LLJ evolution changes drastically with further increase of α. When it reaches 0.18° (case B13 considered in detail in section 5b), the advection of Θ_e results in remixing of the boundary layer ~8 h after sunset, followed by the rapid dissolution of the initial jet and the gradual decay of the

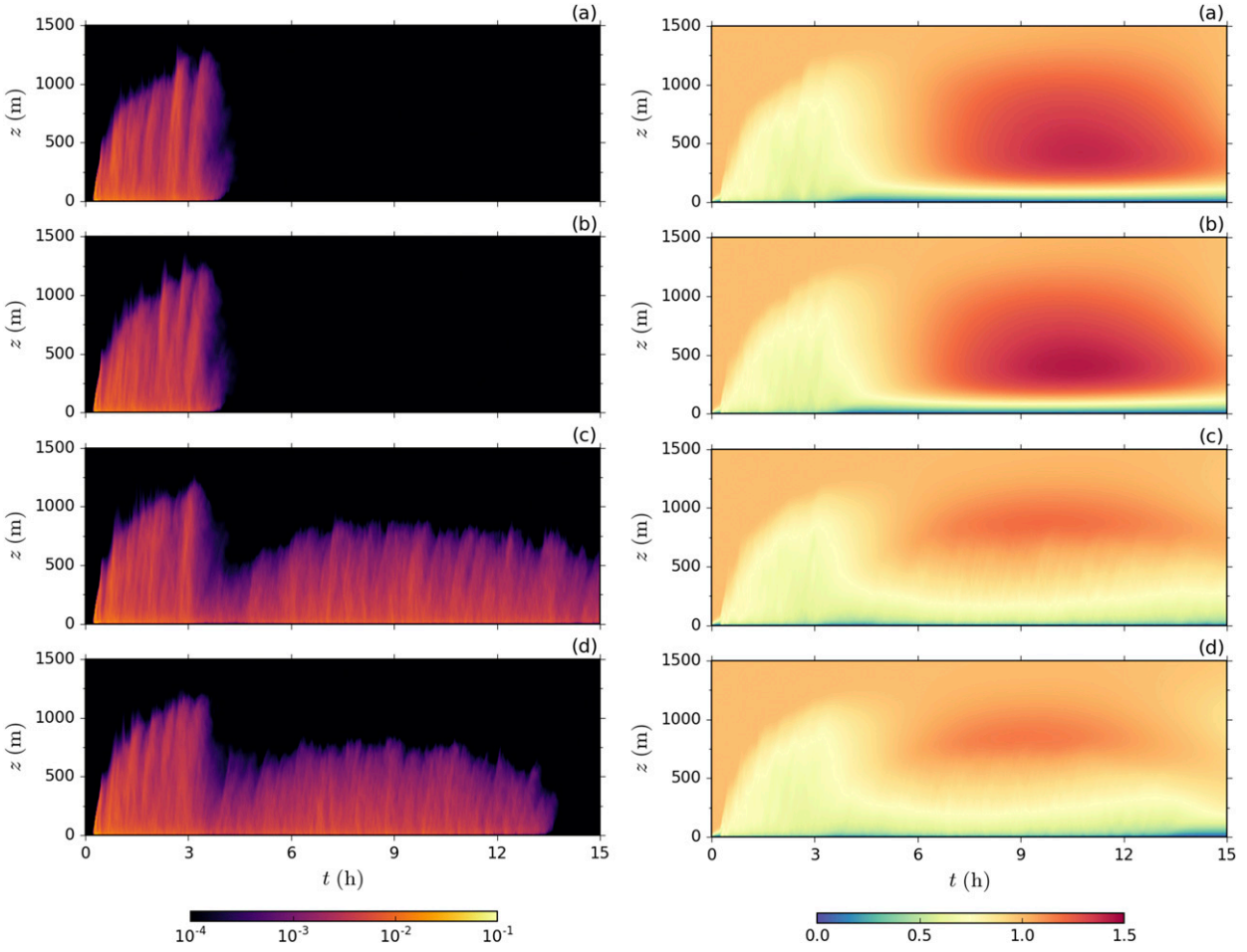

FIG. 15. As in Fig. 14, but for (a) F9 ($\alpha = 0°$), (b) F10 ($\alpha = 0.09°$), (c) F11 ($\alpha = 0.18°$), and (d) F12 ($\alpha = 0.27°$).

residual jet (see discussion of Fig. 12a above). When the slope angle is increased to 0.27°, the turbulence reemergence and remixing of the flow are triggered at an even earlier time, ~5 h into the night. These findings indicate that a shallow slope may play a crucial role in LLJ dynamics, and small variations of the slope angle may considerably affect the evolution and structure of LLJs of the Great Plains, to the extent that overall appearance of the LLJ may be completely changed.

In the experiments with the surface buoyancy-flux forcing (Fig. 15), the effects of the slope on LLJ dynamics are somewhat similar to the slope effects in LLJ cases with the surface buoyancy forcing, but are different in some other respects. For instance, with a very shallow slope (0.09°), the main effect of the slope is the amplification of the nocturnal LLJ due to the previously discussed role of the buoyancy. In this case, the influence of the slope on the redistribution of buoyancy in the lower portion of the boundary layer is minimal. As a result, the flow remains low-turbulent throughout the night, which supports the development of a strong LLJ. However, with $\alpha = 0.18°$ (case F11 discussed in section 5b), a relatively high level of TKE in the lower portion of the boundary layer is retained after the evening transition. This causes formation of a weak elevated jet (Fig. 15c), with the position of the jet maximum closely following the upper boundary of the turbulent layer. With an even steeper slope of 0.27°, the TKE evolution through most of the night is similar to that in the $\alpha = 0.18°$ case. However, at the very end of the night, the persistent upslope advection of Θ_e eventually stabilizes the boundary layer and at some point practically eliminates the resolved TKE within the entire flow.

d. *LLJ development on a slope in the absence of geostrophic wind*

Our preceding analyses have shown that the buoyancy, which develops over a shallow slope as a result of daytime heating, leads to a stronger inertial response and

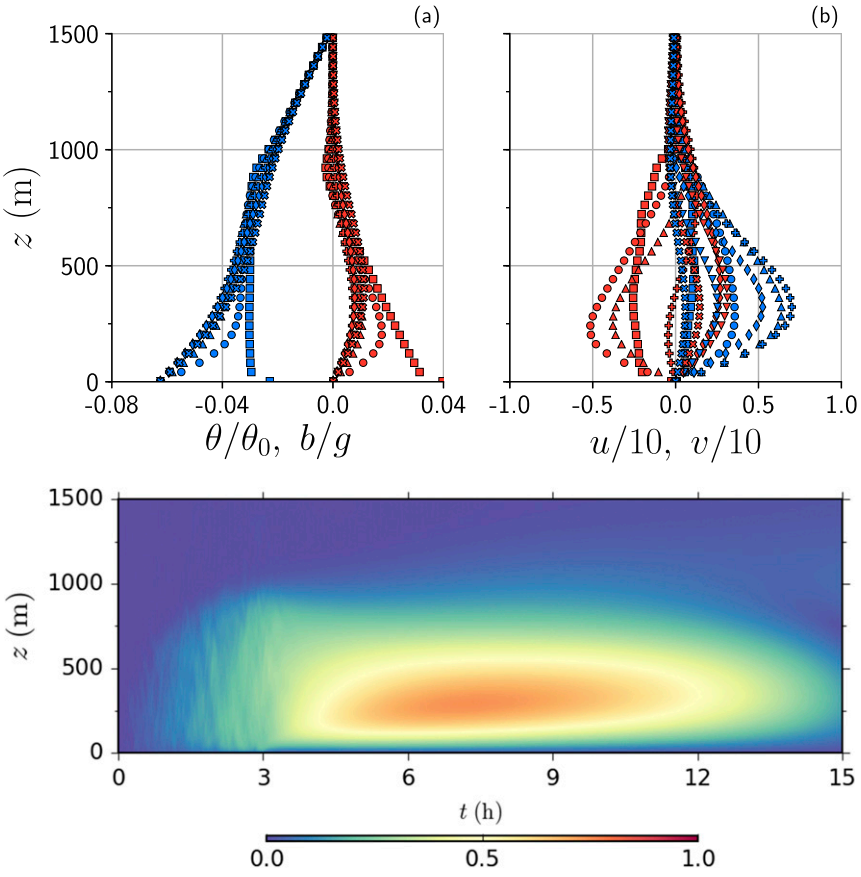

FIG. 16. Normalized profiles of (a) b (red) and potential temperature deviation θ (blue) and (b) u (red) and v (blue) in the LLJ over a shallow slope but without external geostrophic forcing (simulation Z). The corresponding height–time evolution of the wind speed $|V|$ normalized by $10\,\mathrm{m\,s^{-1}}$ is illustrated in the bottom plot. Symbols are as in Fig. 6.

amplifies the southerly LLJ. What will happen if this LLJ driving force, which is closely related to the Holton (1967) mechanism discussed in the introduction and studied in Shapiro et al. (2016), acts in the absence of the free-atmospheric geostrophic forcing when V_g is set to zero? Simulation Z, whose setup is specified in section 4b, has been designed to answer this question. It should be borne in mind that with a homogeneous surface forcing, in the absence of a slope and free-atmosphere geostrophic wind there would not be any mean flow above the ground.

Results from simulation Z with prescribed temporal change of the surface buoyancy are presented in Fig. 16. As in all previously discussed cases, a daytime CBL develops with a well-mixed layer that is characterized by the approximate constancy of potential temperature with height. This convectively mixed boundary layer flow above the slope has nonzero mean components (Fig. 16b). After the release of the frictional constraint and start of the inertial oscillation, the evolving velocity component profiles develop pronounced jetlike shapes. The resulting jet reaches its maximum magnitude of $\sim 8\,\mathrm{m\,s^{-1}}$ at 300 m AGL approximately 4.5 h after sunset. The jet practically disappears toward the end of the simulation (12 h into the night). The stratification in the boundary layer remains generally stable throughout the night; in the lower portion of the layer it changes with time under the influence of the along-slope advection of Θ_e, which switches direction in the middle of the night (see Figs. 16a and 16b).

For a qualitative comparison, the evolving velocity and potential temperature profiles measured at one of the PECAN sites in Kansas under similar conditions of a very weak free-atmosphere geostrophic wind are presented in Fig. 17. These profiles show the same developmental tendencies as their simulated counterparts in Fig. 16.

6. Summary and conclusions

The effects of various external forcings on the evolution and structure of nocturnal LLJs have been

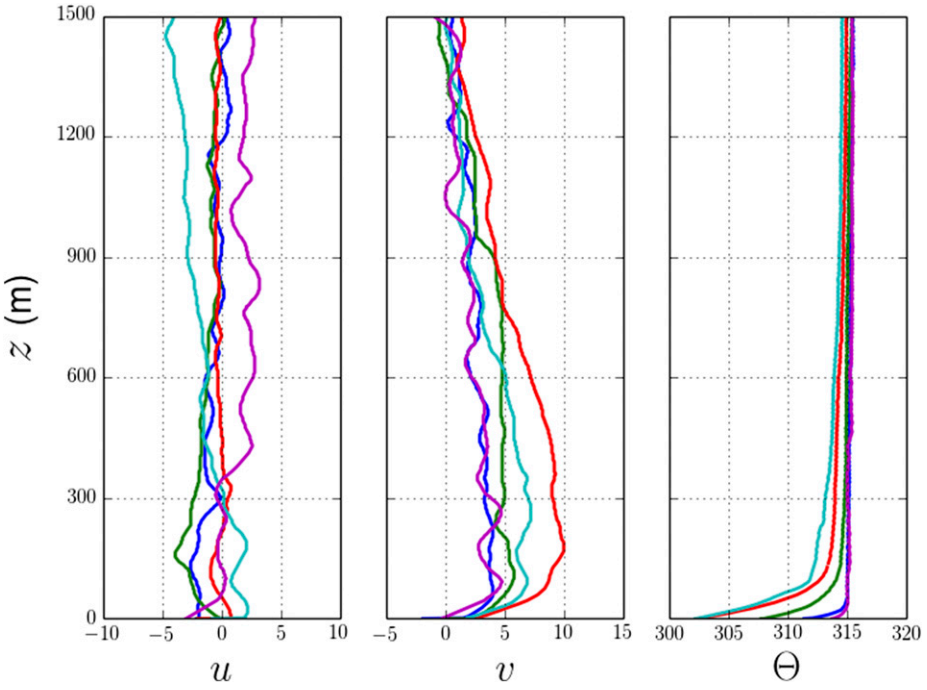

FIG. 17. Profiles of u and v (m s^{-1}) and potential temperature Θ (K) from fixed PECAN Integrated Sounding Array 5 (FP5) in Brewster, Kansas, on 9–10 June 2015 at 2330 UTC (around the time of sunset; purple), 0100 UTC, (blue), 0230 UTC (green), 0530 UTC (red), and 0830 UTC (turquoise). Data source: UCAR/NCAR (2015).

investigated by means of direct numerical simulation. The study has focused on the LLJ type that is characteristic of the U.S. Great Plains, where the jets occur over terrain that gently slopes down from west to east. Over such a slope, the LLJ develops as an inertia–gravity oscillation in a tilted atmospheric boundary layer. The oscillation is initiated by an abrupt change of the surface thermal forcing during the evening transition. In our simulations, this forcing has been prescribed in the form of a surface buoyancy or surface buoyancy flux that is spatially uniform over the slope but change in time. Among other investigated governing parameters are the free-atmosphere geostrophic wind magnitude (this wind is taken southerly in our study), the environmental Brunt–Väisälä (buoyancy) frequency, and the slope angle. LLJs over shallow slopes of different steepness have been contrasted with LLJs over flat terrain.

Each simulation began with the generation of a slope-following daytime CBL driven by the prescribed surface forcing. Under the combined effect of a southerly geostrophic wind and positive surface buoyancy, an upslope component in the CBL flow developed in the afternoon. At sunset, the surface buoyancy (or buoyancy flux) was dropped to a nighttime value. The boundary layer flow adjusted to such a change via an oscillation that had both gravitational (buoyancy) and inertial (associated with weakened near-surface friction) components. The nocturnal LLJ resulting from such an oscillation differed in many aspects from the traditional LLJ typically considered in the flat-terrain context. The shape of the jet wind speed profile over a slope was characterized by a sharper and larger-magnitude maximum.

We now summarize the main findings of our study. First, we documented that the along-slope advection of environmental potential temperature throughout the boundary layer during the night has a major impact on the structure and evolution of the LLJ. In particular, this advection alters the buoyancy field and can reignite static instability in the weakly turbulent LLJ flow. The turbulence that reemerges as result of the instability leads to a complete or partial remix of the lower portion of the boundary layer flow and drastically changes the appearance of the LLJ in terms of its shape and vertical position. Additionally, we confirmed that a pronounced nighttime jetlike flow develops from the daytime tilted CBL in the absence of any free-atmospheric geostrophic forcing.

Acknowledgments. A preliminary version of these results was presented at the 22nd AMS Symposium on Boundary Layers and Turbulence, 20–24 June 2016. We

thank Joshua Gebauer for the construction of plots with PECAN data. We are also thankful to three reviewers for their valuable suggestions on improving the paper. We are especially grateful to the anonymous reviewer who pointed to an error in our plotted turbulence data. This research was supported by the National Science Foundation under Grant AGS-1359698.

REFERENCES

Ansorge, C., and J. P. Mellado, 2014: Global intermittency and collapsing turbulence in the stratified planetary boundary layer. *Bound.-Layer Meteor.*, **153**, 89–116, doi:10.1007/s10546-014-9941-3.

Arritt, R. W., T. D. Rink, M. Segal, D. P. Todey, C. A. Clark, M. J. Mitchell, and K. M. Labas, 1997: The Great Plains low-level jet during the warm season of 1993. *Mon. Wea. Rev.*, **125**, 2176–2192, doi:10.1175/1520-0493(1997)125<2176:TGPLLJ>2.0.CO;2.

Augustine, J. A., and F. Caracena, 1994: Lower-tropospheric precursors to nocturnal MCS development over the central United States. *Wea. Forecasting*, **9**, 116–135, doi:10.1175/1520-0434(1994)009<0116:LTPTNM>2.0.CO;2.

Baas, P., F. C. Bosveld, H. Klein Baltink, and A. A. M. Holtslag, 2009: A climatology of nocturnal low-level jet at Cabauw. *J. Appl. Meteor. Climatol.*, **48**, 1627–1642, doi:10.1175/2009JAMC1965.1.

Banta, R. M., 2008: Stable-boundary-layer regimes from the perspective of the low-level jet. *Acta Geophys.*, **56**, 58–87, doi:10.2478/s11600-007-0049-8.

——, R. K. Newsom, J. K. Lundquist, Y. L. Pichugina, R. L. Coulter, and L. Mahrt, 2002: Nocturnal low-level jet characteristics over Kansas during CASES-99. *Bound.-Layer Meteor.*, **105**, 221–252, doi:10.1023/A:1019992330866.

Blackadar, A. K., 1957: Boundary layer wind maxima and their significance for the growth of nocturnal inversions. *Bull. Amer. Meteor. Soc.*, **38**, 283–290.

Bonner, W. D., 1968: Climatology of the low level jet. *Mon. Wea. Rev.*, **96**, 833–850, doi:10.1175/1520-0493(1968)096<0833:COTLLJ>2.0.CO;2.

——, and J. Paegle, 1970: Diurnal variations in boundary layer winds over the south-central United States in summer. *Mon. Wea. Rev.*, **98**, 735–744, doi:10.1175/1520-0493(1970)098<0735:DVIBLW>2.3.CO;2.

Brook, R. R., 1985: The Koorin nocturnal low-level jet. *Bound.-Layer Meteor.*, **32**, 133–154, doi:10.1007/BF00120932.

Buajitti, K., and A. K. Blackadar, 1957: Theoretical studies of diurnal wind-structure variations in the planetary boundary layer. *Quart. J. Roy. Meteor. Soc.*, **83**, 486–500, doi:10.1002/qj.49708335804.

Clark, R., 2015: FP3 Ellis, KS radiosonde data, version 2.0. UCAR/NCAR Earth Observing Laboratory, accessed 4 January 2017, doi:10.5065/D6GM85DZ.

Coleman, G. N., J. H. Ferziger, and P. R. Spalart, 1990: A numerical study of the turbulent Ekman layer. *J. Fluid Mech.*, **213**, 313–348, doi:10.1017/S0022112090002348.

Cotton, W. R., M.-S. Lin, R. L. McAnelly, and C. J. Tremback, 1989: A composite model of mesoscale convective complexes. *Mon. Wea. Rev.*, **117**, 765–783, doi:10.1175/1520-0493(1989)117<0765:ACMOMC>2.0.CO;2.

Davies, P. A., 2000: Development and mechanisms of the nocturnal jet. *Meteor. Appl.*, **7**, 239–246, doi:10.1017/S1350482700001535.

Deusebio, E., G. Brethouwer, P. Schlatter, and E. Lindborg, 2014: A numerical study of the unstratified and stratified Ekman layer. *J. Fluid Mech.*, **755**, 672–704, doi:10.1017/jfm.2014.318.

Fedorovich, E., and A. Shapiro, 2009a: Turbulent natural convection along a vertical plate immersed in a stably stratified fluid. *J. Fluid Mech.*, **636**, 41–57, doi:10.1017/S0022112009007757.

——, and ——, 2009b: Structure of numerically simulated katabatic and anabatic flows along steep slopes. *Acta Geophys.*, **57**, 981–1010, doi:10.2478/s11600-009-0027-4.

Garcia, J. R., and J. P. Mellado, 2014: The two-layer structure of the entrainment zone in the convective boundary layer. *J. Atmos. Sci.*, **71**, 1935–1955, doi:10.1175/JAS-D-13-0148.1.

Geerts, B., and Coauthors, 2017: The 2015 Plains Elevated Convection at Night (PECAN) field project. *Bull. Amer. Meteor. Soc.*, **98**, 767–786, doi:10.1175/BAMS-D-15-00257.1.

Higgins, R. W., Y. Yao, E. S. Yaresh, J. E. Janowiak, and K. C. Mo, 1997: Influence of the Great Plains low-level jet on summertime precipitation and moisture transport over the central United States. *J. Climate*, **10**, 481–507, doi:10.1175/1520-0442(1997)010<0481:IOTGPL>2.0.CO;2.

Hoecker, W. H., 1963: Three southerly low-level jet systems delineated by the Weather Bureau special pibal network of 1961. *Mon. Wea. Rev.*, **91**, 573–582, doi:10.1175/1520-0493(1963)091<0573:TSLJSD>2.3.CO;2.

Holton, J. R., 1967: The diurnal boundary layer wind oscillation above sloping terrain. *Tellus*, **19**, 199–205, doi:10.1111/j.2153-3490.1967.tb01473.x.

Jiang, X., N.-C. Lau, I. M. Held, and J. J. Ploshay, 2007: Mechanisms of the Great Plains low-level jet as simulated in an AGCM. *J. Atmos. Sci.*, **64**, 532–547, doi:10.1175/JAS3847.1.

Jonker, H. J. J., M. van Reeuwijk, P. P. Sullivan, and E. G. Patton, 2013: On the scaling of shear-driven entrainment: A DNS study. *J. Fluid Mech.*, **732**, 150–165, doi:10.1017/jfm.2013.394.

Klein, P. M., X.-M. Hu, A. Shapiro, and M. Xue, 2016: Linkages between boundary-layer structure and the development of nocturnal low-level jets in central Oklahoma. *Bound.-Layer Meteor.*, **158**, 383–408, doi:10.1007/s10546-015-0097-6.

Marlatt, S., S. Waggy, and S. Biringen, 2012: Direct numerical simulation of the turbulent Ekman layer: Evaluation of closure models. *J. Atmos. Sci.*, **69**, 1106–1117, doi:10.1175/JAS-D-11-0107.1.

Mellado, J. P., 2012: Direct numerical simulation of free convection over a heated plate. *J. Fluid Mech.*, **712**, 418–450, doi:10.1017/jfm.2012.428.

——, C. van Heerwaarden, and J. R. Garcia, 2016: Near-surface effects of free atmosphere stratification in free convection. *Bound.-Layer Meteor.*, **159**, 69–95, doi:10.1007/s10546-015-0105-x.

Mitchell, M. K., R. W. Arritt, and K. Labas, 1995: An hourly climatology of the summertime Great Plains low-level jet using wind profiler observations. *Wea. Forecasting*, **10**, 576–591, doi:10.1175/1520-0434(1995)010<0576:ACOTWS>2.0.CO;2.

Pan, Z., M. Segal, and R. W. Arritt, 2004: Role of topography in forcing low-level jets in the central United States during the 1993 flood-altered terrain simulations. *Mon. Wea. Rev.*, **132**, 396–403, doi:10.1175/1520-0493(2004)132<0396:ROTIFL>2.0.CO;2.

Parish, T. R., and L. D. Oolman, 2010: On the role of sloping terrain in the forcing of the Great Plains low-level jet. *J. Atmos. Sci.*, **67**, 2690–2699, doi:10.1175/2010JAS3368.1.

——, A. R. Rodi, and R. D. Clark, 1988: A case study of the summertime Great Plains low level jet. *Mon. Wea. Rev.*, **116**, 94–105, doi:10.1175/1520-0493(1988)116<0094:ACSOTS>2.0.CO;2.

Pope, S. B., 2000: *Turbulent Flows*. Cambridge University Press, 771 pp.

Shah, S., and E. Bou-Zeid, 2014: Direct numerical simulations of turbulent Ekman layers with increasing static stability: Modifications to the bulk structure and second-order statistics. *J. Fluid Mech.*, **760**, 494–539, doi:10.1017/jfm.2014.597.

Shapiro, A., and E. Fedorovich, 2008: Coriolis effects in homogeneous and inhomogeneous katabatic flows. *Quart. J. Roy. Meteor. Soc.*, **134**, 353–370, doi:10.1002/qj.217.

——, and ——, 2009: Nocturnal low-level jet over a shallow slope. *Acta Geophys.*, **57**, 950–980, doi:10.2478/s11600-009-0026-5.

——, and ——, 2010: Analytical description of a nocturnal low-level jet. *Quart. J. Roy. Meteor. Soc.*, **136**, 1255–1262, doi:10.1002/qj.628.

——, ——, and J. Gibbs, 2015: An analytical verification test for numerically simulated convective flow above a thermally heterogeneous surface. *Geosci. Model Dev.*, **8**, 1809–1819, doi:10.5194/gmd-8-1809-2015.

——, ——, and S. Rahimi, 2016: A unified theory for the Great Plains nocturnal low-level jet. *J. Atmos. Sci.*, **73**, 3037–3057, doi:10.1175/JAS-D-15-0307.1.

Singh, M. P., R. T. McNider, and J. T. Lin, 1993: An analytical study of diurnal wind-structure variations in the boundary layer and the low-level nocturnal jet. *Bound.-Layer Meteor.*, **63**, 397–423, doi:10.1007/BF00705360.

Smagorinsky, J., 1963: General circulation experiments with the primitive equations. *Mon. Wea. Rev.*, **91**, 99–164, doi:10.1175/1520-0493(1963)091<0099:GCEWTP>2.3.CO;2.

Song, J., K. Liao, R. L. Coulter, and B. M. Lesht, 2005: Climatology of the low-level jet at the Southern Great Plains Atmospheric Boundary Layer Experiments site. *J. Appl. Meteor.*, **44**, 1593–1606, doi:10.1175/JAM2294.1.

Spalart, P. R., G. N. Coleman, and R. Johnstone, 2008: Direct numerical simulation of the Ekman layer: A step in Reynolds number, and cautious support for a log law with a shifted origin. *Phys. Fluids*, **20**, 101507, doi:10.1063/1.3005858.

Stensrud, D. J., 1996: Importance of low-level jets to climate: A review. *J. Climate*, **9**, 1698–1711, doi:10.1175/1520-0442(1996)009<1698:IOLLJT>2.0.CO;2.

Stull, R. B., 1988: *An Introduction to Boundary Layer Meteorology*. Kluwer Academic, 666 pp.

Thorpe, A. J., and T. H. Guymer, 1977: The nocturnal jet. *Quart. J. Roy. Meteor. Soc.*, **103**, 633–653, doi:10.1002/qj.49710343809.

Ting, M., and H. Wang, 2006: The role of the North American topography on the maintenance of the Great Plains summer low-level jet. *J. Atmos. Sci.*, **63**, 1056–1068, doi:10.1175/JAS3664.1.

Tuttle, J. D., and C. A. Davis, 2006: Corridors of warm season precipitation in the central United States. *Mon. Wea. Rev.*, **134**, 2297–2317, doi:10.1175/MWR3188.1.

UCAR/NCAR, 2015: FP5 NCAR/EOL QC soundings, version 2.0. UCAR/NCAR Earth Observing Laboratory, accessed 4 January 2017, doi:10.5065/D6ZG6QF7.

Van de Wiel, B. J. H., A. F. Moene, G. J. Steeneveld, P. Baas, F. C. Bosveld, and A. A. M. Holtslag, 2010: A conceptual view on inertial oscillations and nocturnal low-level jets. *J. Atmos. Sci.*, **67**, 2679–2689, doi:10.1175/2010JAS3289.1.

Van Heerwaarden, C., and J. P. Mellado, 2016: Growth and decay of a convective boundary layer over a surface with a constant temperature. *J. Atmos. Sci.*, **73**, 2165–2177, doi:10.1175/JAS-D-15-0315.1.

——, ——, and A. de Lozar, 2014: Scaling laws for the heterogeneously heated free convective boundary layer. *J. Atmos. Sci.*, **71**, 3975–4000, doi:10.1175/JAS-D-13-0383.1.

——, B. J. H. van Stratum, T. Heus, J. A. Gibbs, E. Fedorovich, and J.-P. Mellado, 2017: MicroHH 1.0: A computational fluid dynamics code for direct numerical simulation and large-eddy simulation of atmospheric boundary layer flows. *Geosci. Model Dev.*, doi:10.5194/gmd-2017-41, in press.

Walters, C. K., J. A. Winkler, R. P. Shadbolt, J. van Ravensway, and G. D. Bierly, 2008: A long-term climatology of southerly and northerly low-level jets for the central United States. *Ann. Assoc. Amer. Geogr.*, **98**, 521–552, doi:10.1080/00045600802046387.

Wang, S.-Y., and T.-C. Chen, 2009: The late-spring maximum of rainfall over the U.S. central plains and the role of the low-level jet. *J. Climate*, **22**, 4696–4709, doi:10.1175/2009JCLI2719.1.

Wexler, H., 1961: A boundary layer interpretation of the low-level jet. *Tellus*, **13**, 368–378, doi:10.3402/tellusa.v13i3.9513.

Whiteman, C. D., X. Bian, and S. Zhong, 1997: Low-level jet climatology from enhanced rawinsonde observations at a site in the southern Great Plains. *J. Appl. Meteor.*, **36**, 1363–1376, doi:10.1175/1520-0450(1997)036<1363:LLJCFE>2.0.CO;2.

Williams, O., T. Hohman, T. van Buren, E. Bou-Zeid, and A. J. Smits, 2017: The effect of stable thermal stratification on turbulent boundary layer statistics. *J. Fluid Mech.*, **812**, 1039–1075, doi:10.1017/jfm.2016.781.

Zhong, S., J. D. Fast, and X. Bian, 1996: A case study of the Great Plains low-level jet using wind profiler network data and a high-resolution mesoscale model. *Mon. Wea. Rev.*, **124**, 785–806, doi:10.1175/1520-0493(1996)124<0785:ACSOTG>2.0.CO;2.